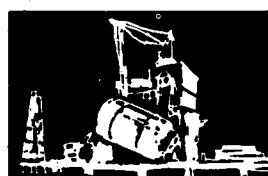
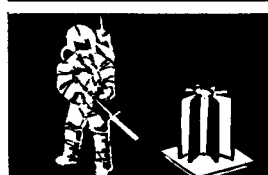
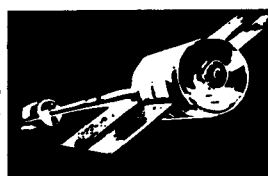
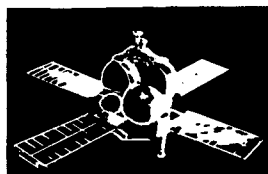
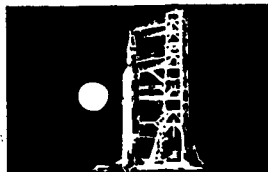
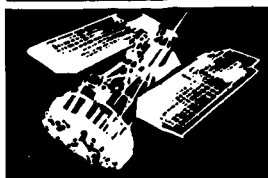


2-p (mix)

# SPACE DIVISION



GE Document No. 72SD4249

November 15, 1972

NTIS

HC \$7.50

## QUARTERLY REPORT NO. 2 FEASIBILITY STUDY OF A 110 WATT PER KILOGRAM LIGHTWEIGHT SOLAR ARRAY SYSTEM

Prepared for:  
Jet Propulsion Laboratory

Prepared Under:  
Contract 953387

(NASA-CR-130287) FEASIBILITY STUDY OF A  
110 WATT PER KILOGRAM LIGHTWEIGHT SOLAR  
ARRAY SYSTEM Quarterly Report, 1 Aug. -  
31 Oct. 1972 (General Electric Co.)  
110 p HC \$7.50

N73-15079

Unclas  
52041

CSCL 10A G3/03

GENERAL  ELECTRIC

Reproduced by  
NATIONAL TECHNICAL  
INFORMATION SERVICE  
US Department of Commerce  
Springfield, VA. 22151

98 PB  
100

GE DOCUMENT NO. 72SD4249  
NOVEMBER 15, 1972

QUARTERLY REPORT NO. 2

FEASIBILITY STUDY  
OF A

110 WATT PER KILOGRAM  
LIGHTWEIGHT SOLAR ARRAY SYSTEM  
1 AUGUST 1972 TO 31 OCTOBER 1972

PREPARED FOR

JET PROPULSION LABORATORY  
CALIFORNIA INSTITUTE OF TECHNOLOGY  
PASADENA, CALIFORNIA

PREPARED UNDER: CONTRACT 953387

JPL PROJECT MANAGER: E. SEGUEIRA

PREPARED BY: N.F. SHEPARD  
C. STAHL  
A. SCHNEIDER  
K.L. HANSON

THIS WORK WAS PERFORMED FOR THE JET  
PROPULSION LABORATORY, CALIFORNIA  
INSTITUTE OF TECHNOLOGY, AS SPONSORED  
BY THE NATIONAL AERONAUTICS AND SPACE  
ADMINISTRATION UNDER CONTRACT NAS7-100

**GENERAL  ELECTRIC**

**SPACE SYSTEMS ORGANIZATION**

Valley Forge Space Center

P. O. Box 8555 • Philadelphia, Penna. 19101

"This report contains information prepared by the General Electric Company, Space Systems Organization, under JPL Subcontract. Its content is not necessarily endorsed by the Jet Propulsion Laboratory, California Institute of Technology, or the National Aeronautics and Space Administration."

## ABSTRACT

This report describes the technical progress during the second quarter of an investigation of the feasibility of a solar array panel subsystem which will produce 10,000 watts of electrical output at 1 A.U. with an overall beginning-of-life power-to-weight ratio of at least 110 watt/kg. A description of the current baseline configuration which meets these requirements is presented. A parametric analysis of the single boom, two blanket planar solar array system was performed to arrive at the optimum system aspect ratio. A novel concept for the stiffening of a lightweight solar array by canting the solar cell blankets at a small angle to take advantage of the inherent in-plane stiffness to increase the symmetric out-of-plane frequency is introduced along with a preliminary analysis of the stiffening effect. /,

A comparison of welded and soldered solar cell interconnections leads to the conclusion that welding is required on this ultralightweight solar array. The status of welded interconnector technology is reviewed. The use of a boron/aluminum composite material in a BI-STEM type deployable boom is investigated as a possible advancement in the state-of-the-art.

## TABLE OF CONTENTS

<u>SECTION</u>		<u>PAGE</u>
1	INTRODUCTION AND SUMMARY . . . . .	1-1
2	TECHNICAL DISCUSSION . . . . .	2-1
	2.1 The Current Baseline Configuration . . . . .	2-1
	2.1.1 General Description . . . . .	2-1
	2.1.2 Structural Design . . . . .	2-5
	2.1.3 Solar Cell Blanket Construction . . . . .	2-8
	2.2 Parametric Analysis of a Planar Solar Array . . . . .	2-14
	2.2.1 Aspect Ratio Trade Study . . . . .	2-14
	2.2.2 Solar Cell Blanket Configuration Trade-offs . . . . .	2-25
	2.3 Comparison of Deployable Boom Types . . . . .	2-36
	2.4 Analysis of "V"-Stiffened Solar Array . . . . .	2-39
	2.4.1 Introduction . . . . .	2-39
	2.4.2 RA250 In-Phase Test Analysis . . . . .	2-41
	2.4.3 Symmetric Vibration Analysis . . . . .	2-43
	2.4.4 Assessment of Stiffening Effects . . . . .	2-47
	2.4.5 Assessment of Reduced Stiffness . . . . .	2-51
	2.5 Advances in the State-of-the-Art . . . . .	2-54
	2.5.1 Introduction . . . . .	2-54
	2.5.2 Boron/Aluminum BI-STEM . . . . .	2-54
	2.5.3 Welded Solar Cell Interconnections . . . . .	2-68
3	CONCLUSIONS . . . . .	3-1
4	RECOMMENDATIONS . . . . .	4-1
5	NEW TECHNOLOGY . . . . .	5-1
6	REFERENCES . . . . .	6-1

## LIST OF ILLUSTRATIONS

<u>FIGURE</u>		<u>PAGE</u>
1	Outline Drawing of Current Baseline Configuration . . . . .	2-3
2	Details of Module Arrangement on Solar Cell Blankets . . . . .	2-9
3	Circuit I-V Characteristic . . . . .	2-10
4	Typical Section through the Blanket at the Edge . . . . .	2-13
5	Finite-Element Model of Two Blanket, Single Boom Solar Array . . . . .	2-15
6	Boron/Aluminum BI-STEM Weight and Diameter as a Function of Bending Stiffness . . . . .	2-17
7	Molybdenum BI-STEM Weight and Diameter as a Function of Bending Stiffness . . . . .	2-17
8	Symmetric and Anti-symmetric Frequency vs. Tension . . . . .	2-19
9	Symmetric and Anti-symmetric Frequency vs. Tension . . . . .	2-19
10	Optimum Boom Stiffness and Tension vs. Frequency . . . . .	2-20
11	Optimum Boom Stiffness and Tension vs. Frequency . . . . .	2-22
12	BI-STEM Deployer Weight vs. Boom Diameter . . . . .	2-23
13	Total Structural Weight vs. Blanket Width and Strip Length . . .	2-24
14	Total System Weight vs. Deployed Natural Frequency . . . . .	2-26
15	Total System Weight vs. Deployed Natural Frequency . . . . .	2-26
16	Total System Weight vs. Aspect Ratio . . . . .	2-27
17	Total System Weight vs. Aspect Ratio . . . . .	2-27
18	Solar Cell Circuit Configuration . . . . .	2-29
19	Solar Cell Blanket Configuration . . . . .	2-31
20	Comparison of 2 and 10 ohm-cm Cells at Various Operating Temperatures . . . . .	2-33
21	Comparison of Deployable Boom Types . . . . .	2-36
22	"V" Configuration, Single Boom Solar Array Concept . . . . .	2-39

# LIST OF ILLUSTRATIONS (Cont'd)

<u>FIGURE</u>		<u>PAGE</u>
23	In-plane Force-Deflection Characteristic . . . . .	2-42
24	Symmetric Models . . . . .	2-44
25	Edge View of Deflected Array . . . . .	2-46
26	Force Diagram of Outer End of Array . . . . .	2-46
27	Effect of Blanket Tension on Solar Array Frequency . . . . .	2-50
28	Effect of Boom Stiffness on "V" Configuration Solar Array Characteristic . . . . .	2-53
29	Effect of Fiber Content on Composite Modulus of Elasticity . . . . .	2-60
30	Transverse Elastic Modulus vs. Content of 107 $\mu\text{m}$ BORSIC Fibers . . . . .	2-61
31	Transverse Tensile-Strength of 50% Volume 107 $\mu\text{m}$ BORSIC/Aluminum . . . . .	2-62
32	Transverse Tensile Strength of 60% by Volume 142 $\mu\text{m}$ BORSIC/6061 Aluminum . . . . .	2-63
33	B/Al Composite Tape Material . . . . .	2-64
34	Possible Configurations of B/Al Monolayer Tape . . . . .	2-65
35	BI-STEM Section . . . . .	2-66
36	Normal Cumulative Number of Solder Joints Showing Cracks after 400 Cycles from 75°C to the Indicated Lower Temperature Limit . . . . .	2-69
37	Contact Pull Strength Tab Configuration . . . . .	2-70
38	Contact Strength of Solar Cell Solder Joint . . . . .	2-71
39	Time to Solder Joint Rupture Versus Applied Stress for Two Solder Alloys at Various Temperatures . . . . .	2-71
40	TRW Welded Aluminum Interconnector Configuration . . . . .	2-72
41	Thermal Stress in Welded Joints . . . . .	2-74
42	Cycles to Failure Versus Temperature Range . . . . .	2-74

# LIST OF ILLUSTRATIONS (Cont'd)

<u>FIGURE</u>		<u>PAGE</u>
43	Hughes Aluminum Cell/Aluminum Interconnector Ultrasonically Welded Module . . . . .	2-75
44	Welded Ag Mesh Interconnector . . . . .	2-76
45	Photomicrograph of Welded Joint . . . . .	2-77
46	Hughes MCW-550 Impulse Welder . . . . .	2-77
47	Mechanical Strength of Weld and Electrical Degradation Versus Welding Voltage . . . . .	2-78
48	Laser Microwelder . . . . .	2-79
49	Results of Peel Tests on Thermal-Diffusion Bonded Solar Cell Joints . . . . .	2-80



# LIST OF TABLES

<u>TABLE</u>		<u>PAGE</u>
1	Significant Design Features of the Current Baseline Solar Array Panel Configuration . . . . .	2-1
2	Total System Weight Summary . . . . .	2-5
3	Component Quantity Related to Level of Assembly . . . . .	2-11
4	Design Characteristics of Ferranti Type MS36 125 $\mu$ m Thick Solar Cells . . . . .	2-11
5	Weight Breakdown for Solar Cell Blankets . . . . .	2-14
6	Possible Module Lengths . . . . .	2-32
7	Possible Circuit Arrangements for $N_{S/C} = 540$ . . . . .	2-34
8	Possible Blanket Configurations for $N_{P/M} N_{C/B} = 221$ . . . . .	2-35
9	Possible Blanket Configurations for $N_{P/M} N_{C/B} = 210$ . . . . .	2-37
10	Effect of Blanket Tension on Force-Deflection Characteristics of "V" Configuration Solar Array . . . . .	2-49
11	Effect of Boom Stiffness on Force-Deflection Characteristics of "V" Configuration Solar Array . . . . .	2-52
12	Axial Tensile Strength of 142 $\mu$ m BORSIC/Al . . . . .	2-59
13	Properties of Aluminum Alloy Matrix Materials . . . . .	2-67
14	Comparison of Soldered and Welded Solar Cell Interconnections . . . . .	2-69

SECTION 1  
INTRODUCTION AND SUMMARY

A program to study the feasibility of a 10,000 watt solar array panel system with an overall power-to-weight\* ratio of better than 110 watts/kg was initiated on May 5, 1972. This panel system would be one element of a multipanel solar array system on space vehicles for interplanetary, synchronous earth orbit, or manned space station missions. The power-to-weight ratio is interpreted to be the delivered beginning-of-life maximum power output at 1 AU divided by the total system weight which includes all elements of the deployment and support structure and mechanisms, but not the gimbaling or orientation related equipment. Thus, for the specified power output of 10,000 watts at 1 AU, the total panel system weight must be less than 90.9 kg.

The program has been organized into the following tasks:

<u>Task No.</u>	<u>Task Title</u>
1000	Design Requirements Definition and Analysis
2000	Investigation of Existing Array Technology
3000	Feasibility of Extending Existing Array Concepts to 110 Watts/kg
4000	Definition and Analysis of Improved Configurations
5000	State-of-the-Art Analysis, Projection and Advances

---

\* Throughout this report, the term "weight" is used as a synonym for the term "mass."

In Task 1000 the design requirements for each of the three missions were investigated with the results summarized in the first quarterly report (Reference 1). This set of design requirements was used as a guide to the trade-off and analysis activity during the second quarter.

In Tasks 2000 and 3000, the use of existing concepts, configurations and technology was investigated. The best features of these existing concepts were combined with recent advances in component technology to formulate a baseline configuration which has a power-to-weight ratio of better than 110 watt/kg. This configuration, which is described in Section 2.1, does not require advances in the state-of-the-art to achieve this weight goal.

Task 4000 involves the synthesis of advanced concepts and configurations to meet the system requirements. A promising new concept, called the "V" stiffened solar array, is described in Section 2.4. This concept provides increased stiffness to out-of-plane bending when compared to an equivalent planar geometry. This may allow a reduction in the boom stiffness (and weight) required to maintain a specified deployed natural frequency.

Task 5000 consists of two major parts. One is concerned with the analysis and definition of the state-of-the-art with respect to the design of the candidate configurations. It is a goal of the study to base the design of the system upon component or device performance which has been at least demonstrated in the laboratory. For example, the use of ultrathin ( $\leq 125 \mu\text{m}$  thick) solar cells with integral coverglass and welded interconnectors is considered to be within the current state-of-the-art. The second part of this task is to define desirable advances in the state-of-the-art and to assess the performance payoffs that

result. An example of one such advance is the boron/aluminum BI-STEM type deployable boom which is discussed in Section 2.5.2. The development of such a boom would allow a weight competitive alternative to the continuous longeron ASTROMAST at a lower actuator height.

The second quarter activity has emphasized the formulation of a baseline configuration which has a power-to-weight ratio of better than 110 watt/kg. The parameter analysis which leads to the selection of an optimum aspect ratio is presented in Section 2.2.

## SECTION 2

### TECHNICAL DISCUSSION

#### 2.1 THE CURRENT BASELINE CONFIGURATION

##### 2.1.1 GENERAL DESCRIPTION

A baseline configuration for a solar array panel was synthesized to represent the current design solutions which enable the 110 watt/kg goal to be achieved. This so-called "baseline configuration" will be updated and revised as the program continues.

This current configuration for the solar array panel system is shown in Figure 1 with the significant design features summarized in Table 1. The concept is a

Table 1. Significant Design Features of  
the Current Baseline Solar Array  
Panel Configuration

Parameter	Value
1. Deployed length (L')	18.565 m
2. Total width (W)	5.915 m
3. Blanket width (w)	2.830 m
4. System aspect ratio (L'/W)	3.14
5. Total gross blanket area	105.08 m <sup>2</sup>
6. Total number of solar cells (2 x 2 cm)	226,800
7. Lowest deployed natural frequency	.04 Hz
8. Electrical power output at $V_{mp} = 200$ vdc	10,000 watts
<ul style="list-style-type: none"> <li>• Beginning-of-life (BOL)</li> <li>• 55°C</li> <li>• 1 AU, AMO illumination</li> <li>• Measured at panel interface connector</li> </ul>	
9. Expected maximum power degradation after 3 year interplanetary mission	30%
10. Total system weight	84.1 kg
11. BOL power-to-weight ratio	119 watt/kg
12. EOM power-to-weight ratio	83.2 watt/kg

single, central deployable boom which supports two flexible solar cell blankets. Tension in the solar cell blanket substrates maintains the deployed natural frequency above the minimum specified value of .04 Hz. The flexible solar cell blankets are stowed for launch by folding into a flat-pack package which is retained in compression between a bottom honeycomb panel and spring driven hinged honeycomb panel doors on the top. These doors are held closed during launch by the tubular leading edge member (LEM) which is attached to the deployable boom at the center and retained at each end by a launch retention cable mechanism. Solar array deployment is accomplished by firing redundant cable cutters at each end of the array which releases the end of the LEM as well as releasing the restraint at each end of the supporting truss work. Application of power to the deployable boom actuator will cause the LEM to move off the door panels allowing them to swing open. Continued deployment of the boom will cause the LEM to pull each fold of the blankets from the stowed package. Interlayer cushions of Kapton H film are retained by the bottom panel. At the end of the deployment travel, the further deployment of the blankets applies the required tension load by extending a spring mechanism at the base of each blanket.

A weight summary for the current baseline configuration is given in Table 2. The calculated system weight of 84.1 kg results in a power-to-weight ratio of 119 watt/kg at beginning-of-life. Viewed another way, this weight allows for a 6.8 kg (8.1%) growth margin based on the specified 110 watt/kg goal.

Page intentionally left blank

Table 2. Total System Weight Summary

ITEM		WEIGHT (kg)
Solar Array Blankets		48.5
Stowage and Support Structure		27.6
Frame	7.7	
Container Bottom	4.4	
Container Cover	4.0	
Container Mechanisms	0.1	
Center Fitting	0.8	
Leading Edge Member	2.6	
End Retention Fittings	1.0	
End Retention Cable Cutters	0.9	
End Retention Mechanisms	0.4	
Blanket Tension Mechanisms	1.2	
Interlayer Cushioning	2.5	
Container Foam	1.8	
Coatings	0.1	
Fasteners	0.1	
Deployment Mechanism		8.0
Deployable Boom	2.8	
Actuator	5.2	
		84.1
System power-to-weight ratio = 119 watt/kg		
Growth margin available to achieve 110 watt/kg goal = 6.8 kg (8.1%)		

## 2.1.2 STRUCTURAL DESIGN

### 2.1.2.1 Frame

The frame is a 5.9 m x 0.63 m x 0.31 m welded truss constructed from 2.5 cm and 1.9 cm O.D. by 0.13 cm wall thickness magnesium tubing. The members are sized to resist buckling under a 6.5 g load in the direction of deployment.

### 2.1.2.2 Blanket Stowage

The blanket is stowed in the upper end of the 0.31 m deep frame between the floor and the covers. The floor consists of a 1.9 cm thick, lightweight honeycomb which is supported by 1.3 cm O.D. by 0.13 cm wall thickness magnesium tubing.

**Preceding page blank**



#### 2.1.2.3 Covers

The two covers extend the full length of the frame, are hinged at one side, and have a small gap between them at the other side. They are fabricated from 0.6 cm thick, lightweight honeycomb which is stiffened by five, equally spaced, magnesium channels. The covers are held in the closed position by means of a leading edge member which meets within cut-outs in the five channels. Springs at the hinge axes open the covers when the leading edge member is deployed.

#### 2.1.2.4 Leading Edge Member

The leading edge member is a 4.4 cm x 7.6 cm x 0.1 cm rectangular, beryllium tube that extends the full length of the frame. The leading edge member provides the dual functions of retaining the covers and blanket in the stowed configuration and of providing the required stiffness for blanket support in the deployed configuration. The member is attached to the boom at its center by means of a bearing support and to the retention cables by means of grooved fittings at both ends.

#### 2.1.2.5 Center Fitting

The center fitting is a welded and machined magnesium member that provides a mounting location for the boom and an interface with the vehicle solar array drive.

#### 2.1.2.6 End Retention

In addition to the center fitting, the frame is retained to the vehicle at its four corners. Two cables, one at each end, preload the frame against four pins attached to the vehicle. One of these pins is tapered and engages a tapered hole to take out lateral loads in both directions. A second, tapered pin en-

gages a tapered slot to take out lateral loads in one direction only. The remaining two pins bear against the frame, but do not take lateral loads. The frame is released by cutting the cables with redundant cable cutters. Cutting the cables releases the leading edge member and allows the four pins to retract thereby releasing the frame.

#### 2.1.2.7 Tension Device

The lower end of each blanket is fastened to a tension tube which is fabricated from 1.9 cm O.D. x 0.08 cm wall beryllium tubing. Each tension tube provides tension to the blanket by means of two relatively constant force springs. The tubes are constrained to move in a linear motion by means of ball bushings at both ends of each tube.

#### 2.1.2.8 Interlayer Cushioning

In the stowed configuration, each layer of the solar cell blanket is separated from the adjacent fold by a 25  $\mu\text{m}$  thick sheet of Kapton-H film. These separators are attached to the frame at one end so as to remain fixed when the blanket deploys. A layer of foam is placed between the top layer of blanket and the covers to equalize load distribution and to retain the blanket during powered flight vibration.

#### 2.1.2.9 Deployable Boom

The deployable boom portion of the system can be implemented with a 17.8 cm (7 inch) diameter continuous fiberglass longeron coilable lattice ASTROMAST. With a motor driven canister which deploys a fully formed mast, the total weight will be 8.0 kg (17.6 lb) for a 18.57 m (60.9 ft) long mast with a bending stiffness of  $3447 \text{ N-m}^2$  (8,350 lb-ft<sup>2</sup>). The deployment canister will be about 86 cm

(34 inches) high by 23 cm (9 inches) in diameter. Another approach might use a boron/aluminum composite BI-STEM type boom element which is discussed in Section 2.5.2. This advanced approach uses a  $178\text{ }\mu\text{m}$  (.007 inches) thick boron/aluminum monolayer tape material to fabricate a 5.34 cm (2.10 inch) diameter BI-STEM type boom with the same bending stiffness of  $3447\text{ N-m}^2$  (8,350 lb-ft<sup>2</sup>). The calculated weight of this deployable boom unit is also 8.0 kg (17.6 lb) including the actuator.

### 2.1.3 SOLAR CELL BLANKET CONSTRUCTION

Each solar cell blanket consists of an interconnection of 30 identical strips as shown in Figure 2. Each strip consists of two series connected solar cell modules, with each module being composed of 1890 2 x 2 cm solar cells which are interconnected 135 in series by 14 in parallel as shown in Figure 2. The two modules on one strip are connected in electrical series with the two modules on an adjacent strip to form a complete electrical circuit. Thus each electrical circuit is composed of 7560 cells connected 540 in series by 14 in parallel. Figure 3 shows the calculated beginning-of-life I-V characteristic for a circuit on the baseline solar array. Each circuit has a calculated 340 watt maximum power output at 200 vdc measured at the circuit terminals. If a 2-percent bus strip distribution loss is accounted for, the total calculated panel output is 9996 watts measured at the panel interface connector. Table 3 is a summary of the component quantities as related to the level of assembly of the panel.

The solar cells are nominal  $125\text{ }\mu\text{m}$  thick, 2 x 2 cm, N/P silicon with a nominal base resistivity of 10 ohm-cm. Table 4 summarizes the significant characteristics of this cell. The solar cells are shielded from the damaging effects of

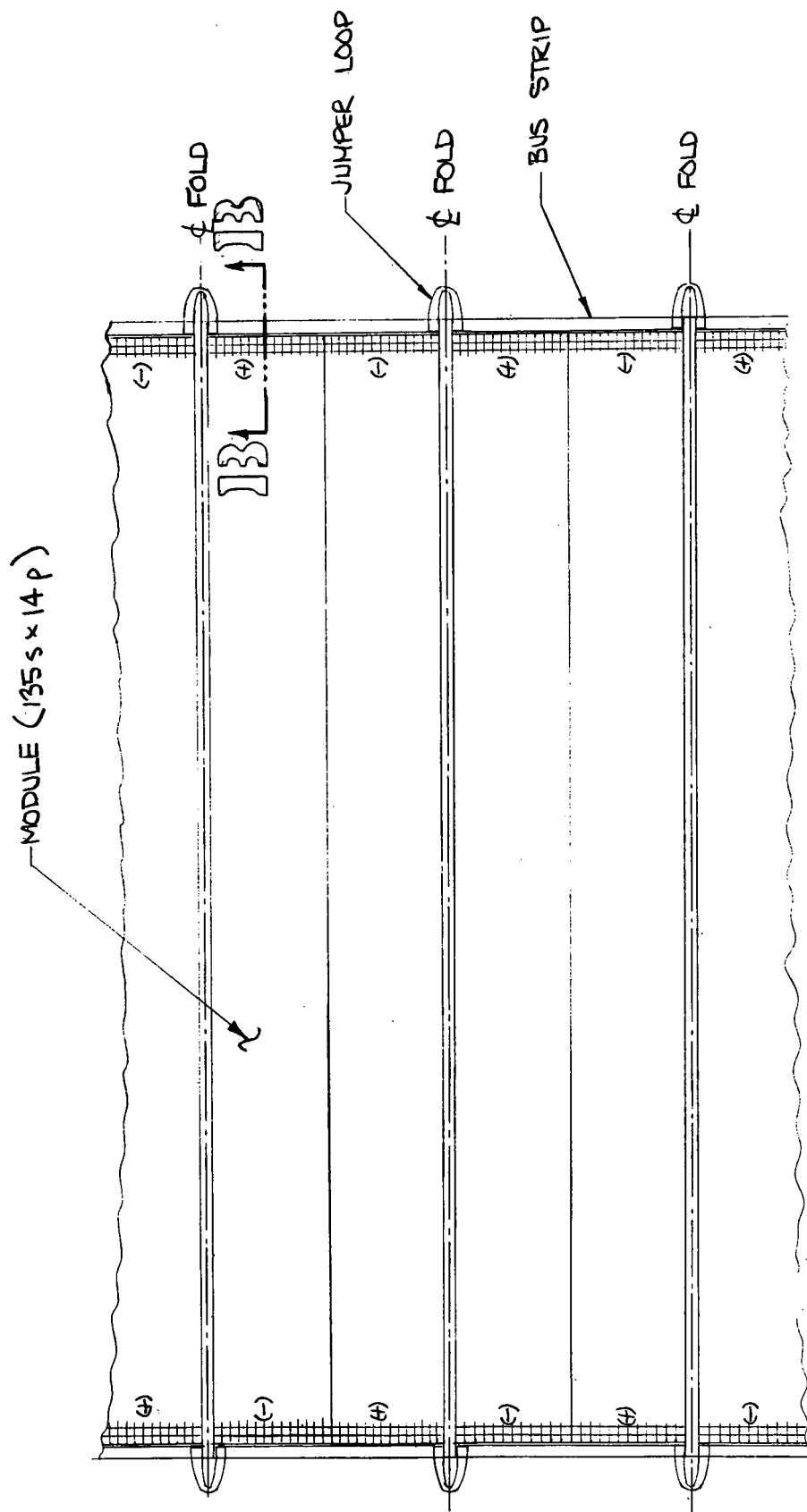


Figure 2. Detail of Module Arrangement on Solar Cell Blankets

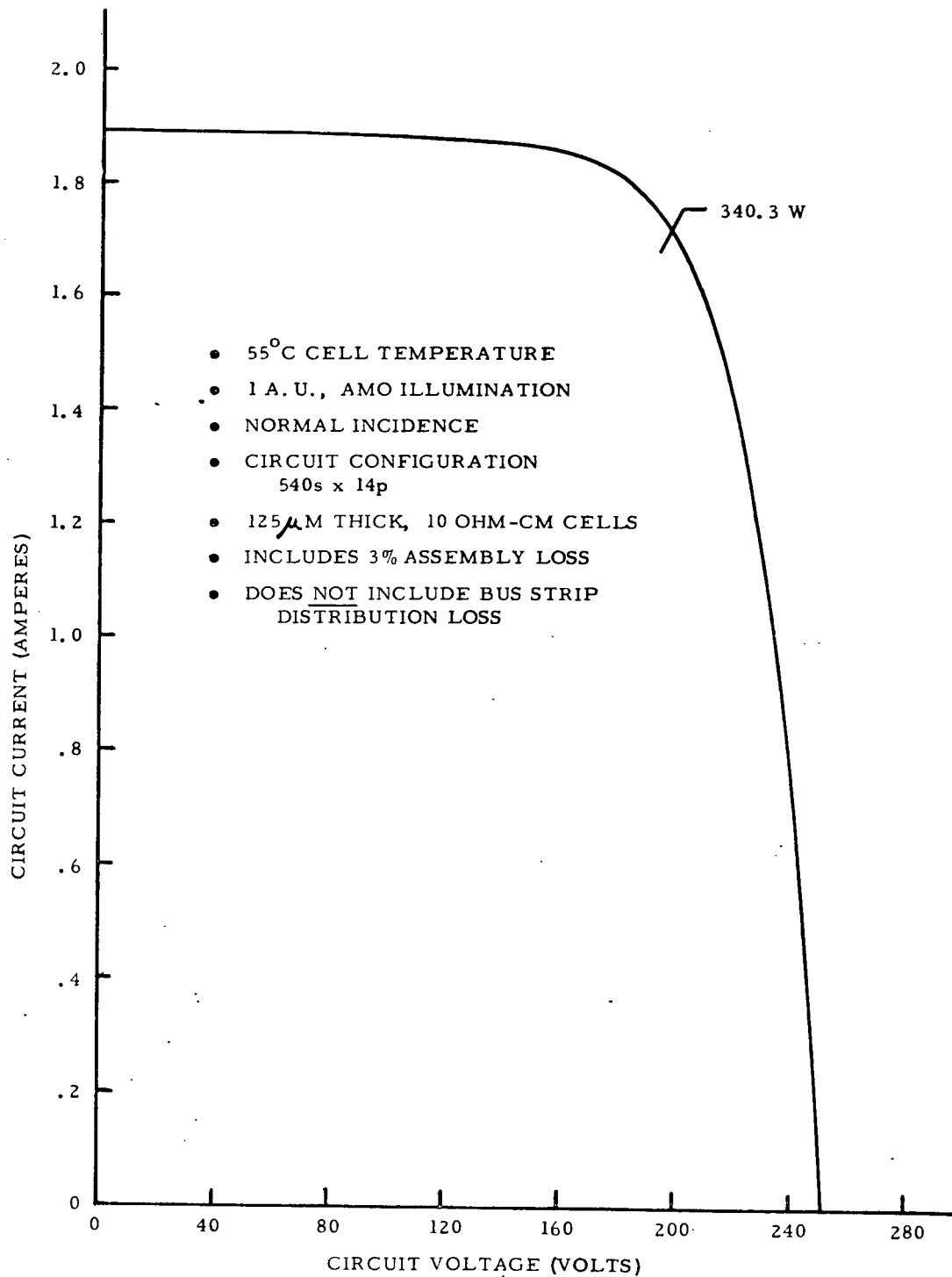


Figure 3. Circuit I-V Characteristic

Table 3. Component Quantity Related to Level of Assembly

	Cell	Module	Strip	Circuit	Blanket	Panel
Cell	1					
Module	1890	1				
Strip	3780	2	1			
Circuit	7560	4	2	1		
Blanket	113,400	60	30	15	1	
Panel	226,800	120	60	30	2	1

Table 4. Design Characteristics of Ferranti Type MS 36  
125  $\mu$ m Thick Solar Cells (from Reference 1)

Feature	Description
Thickness	125 $\pm$ 25 $\mu$ m
Size	20 $\pm$ 0.15 x 20 $\pm$ 0.15 mm
Resistivity	7 to 12 ohm-cm Float zone silicon
Contact Configuration	Bottom wrap-around 24 finger grid geometry
Contact Material	Plated - nickel, copper, nickel, gold
Anti-reflective Coating	TiO <sub>x</sub>
Minimum Lot Average Electrical Performance (covered)	123 ma at 0.445 volts (equivalent AM0, 1 A.U. illumination at 25 $\pm$ 2°C)
Maximum Lot Average Cell Weight	0.129 gm/cell

low energy protons by the deposition of an integral cover of Corning 7070 glass. A nominal integral coverglass thickness of  $37\text{ }\mu\text{m}$  should provide the necessary protection within the weight constraints of this program .

Figure 4 shows a detail of a typical section through the blanket at the edge (section B-B on Figure 1). The solar cells are attached to the Kapton-H film substrate by the interconnectors which are welded to the cell contacts through holes in the substrate. The interconnectors are nominal  $25\text{ }\mu\text{m}$  thick gold plated molybdenum. The bus strips, which run on the sun side of the substrate along each edge, consist of flat copper conductors with Kapton-H film used as the insulator. The electrical connections between blanket strips are made by jumper loops which attach one bus strip segment to the adjacent bus strip segment. The installation of these jumper loops is shown in Figure 2. The fold hinge between blanket strips consists of a strip of FEP-Teflon which is heat sealed to the Kapton substrate to form a lap joint along the width of the blanket.

A detailed weight breakdown for the solar cell blanket is given in Table 5.

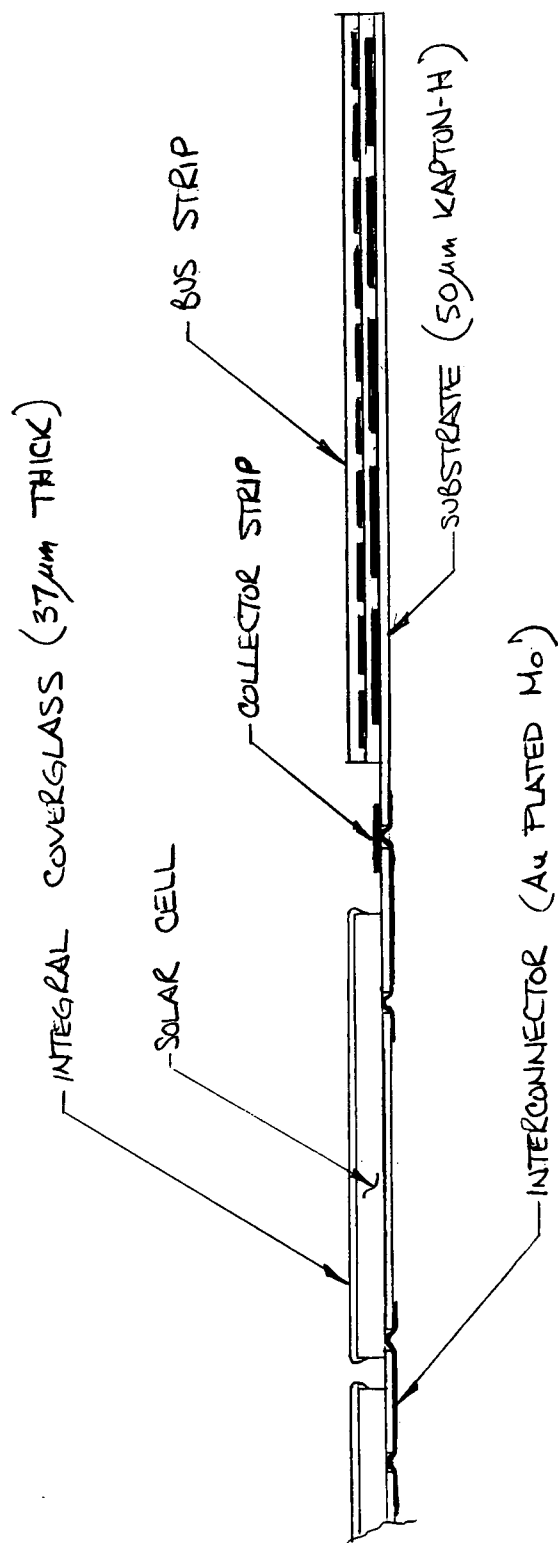


Figure 4. Typical Section through the Blanket at the Edge



Table 5. Weight Breakdown for Solar Cell Blanket  
(Total for both blankets)

Items	Weight (kg)
Solar Cells (.129 gm each)	29.26
Integral Coverglass	7.26
Interconnectors (.008 gm each)	1.81
Substrate	7.54
Bus Strips and Insulators	1.50
Inboard and Outboard Leaders	0.27
Circuit Terminations	0.15
Strip Hinge Joints and Bus Strip Jumpers	<u>0.71</u>
	48.5

## 2.2 PARAMETRIC ANALYSIS OF A PLANAR SOLAR ARRAY

### 2.2.1 ASPECT RATIO TRADE STUDY

Parametric studies which relate total system weight to aspect ratio were performed to determine the optimum solar array geometry for a specified minimum deployed frequency requirement. The first part of this task consisted of determining the minimum boom bending stiffness and blanket tension required to meet the frequency requirement.

#### 2.2.1.1 Optimum Boom and Blanket Tension Analysis

Two deployable boom configurations were considered in this trade study. The first is a boron/aluminum composite BI-STEM boom with a d/t ratio of 300 and an overlap factor of 0.90. For this boom configuration, there is a lower limit to boom size which is determined by a minimum composite monolayer tape thickness

of 178  $\mu\text{m}$ . Thus, with a d/t ratio of 300, the boom diameter cannot be less than 5.33 cm which restricts the bending stiffness to greater than 3447 N-m<sup>2</sup>. From the dynamic standpoint, the continuous longeron ASTROMAST behaves almost identically to the boron/aluminum BI-STEM since for a given bending stiffness, the boom weights per unit length are nearly identical. The second configuration uses a molybdenum BI-STEM boom with a d/t ratio of 200 and an overlap factor of 0.90.

The dynamics analysis required to determine the optimum boom stiffness and tension was performed using a discrete parameter model used for previous RA250 analyses and verified by test. The model used a five by two discretization as shown in Figure 5. Because of the symmetry of the solar array configuration, only half the array was analyzed with appropriate boundary conditions to determine either the symmetric or antisymmetric array modes. Each blanket was repre-

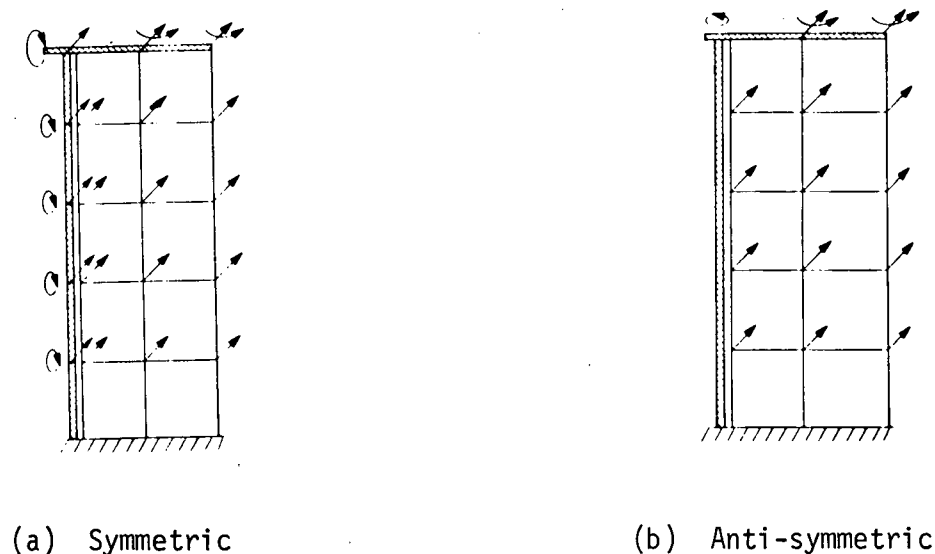


Figure 5. Finite-Element Model of Two Blanket,  
Single Boom Solar Array

sented by 10 rectangular elements that describe the out-of-plane stiffness caused by the blanket tension. The leading edge member (LEM) and boom were modeled using beam elements and included the effect of axial preload on the boom stiffness. The leading edge member was free to rotate relative to the boom about the longitudinal axis of the array. A consistent mass representation was used. The boom density was varied in accordance with the boom stiffness as shown in Figures 6 and 7 for the boron/aluminum and molybdenum booms, respectively. The analyses were performed using the appropriate subroutines in a DYNAMO II program that enabled the parameters to be varied over the range of interest.

The optimization of the blanket tension and boom stiffness for each aspect ratio and frequency was accomplished in two steps. First, the required blanket tension to obtain a desired antisymmetric frequency was determined. Because the LEM is free to rotate about the boom axis, the boom stiffness does not affect the antisymmetric or torsional frequency of the array. Therefore, by varying the blanket tension, the required tension for the desired torsional frequency was first determined. For the required blanket tension, a symmetric vibration analysis was then performed for various values of boom stiffness. Based on previous studies, it was estimated that the boom stiffness would correspond to that required to provide approximately 25 percent of critical buckling under the blanket tension load. Therefore, the symmetric array frequencies were determined for boom stiffnesses corresponding to 22 and 26 percent of critical buckling. A linear interpolation was then used to estimate the boom stiffness for the desired array frequency. The final boom stiffness was then bounded by interpolating between the third frequency and each of the other two frequencies. In general, the bounds of the boom stiffness were within a few percent. Using this approach, an array design having equal symmetric and antisymmetric frequencies was obtained as in

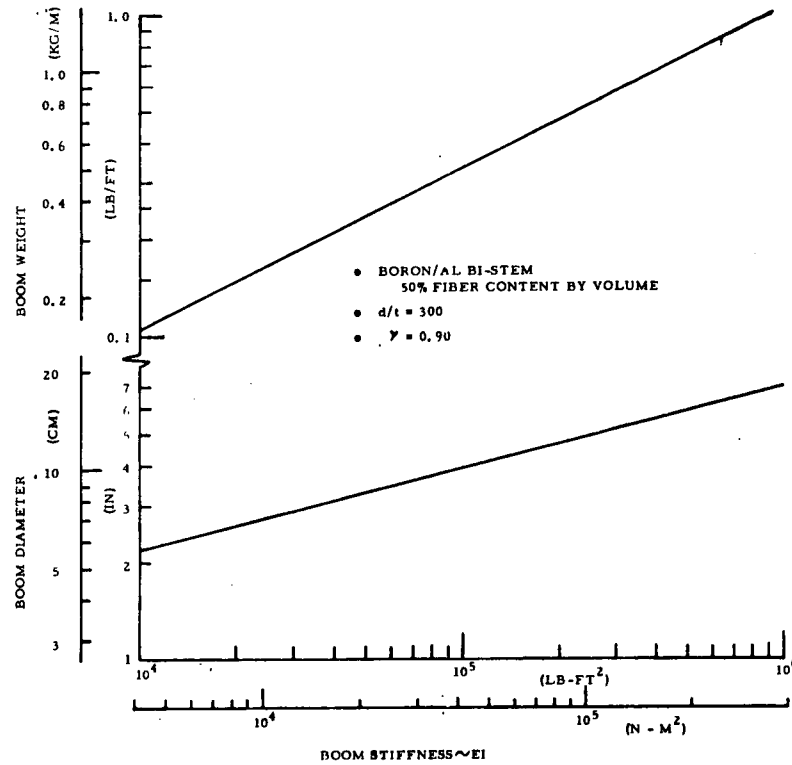


Figure 6. Boron/Aluminum BI-STEM Weight and Diameter as a Function of Bending Stiffness

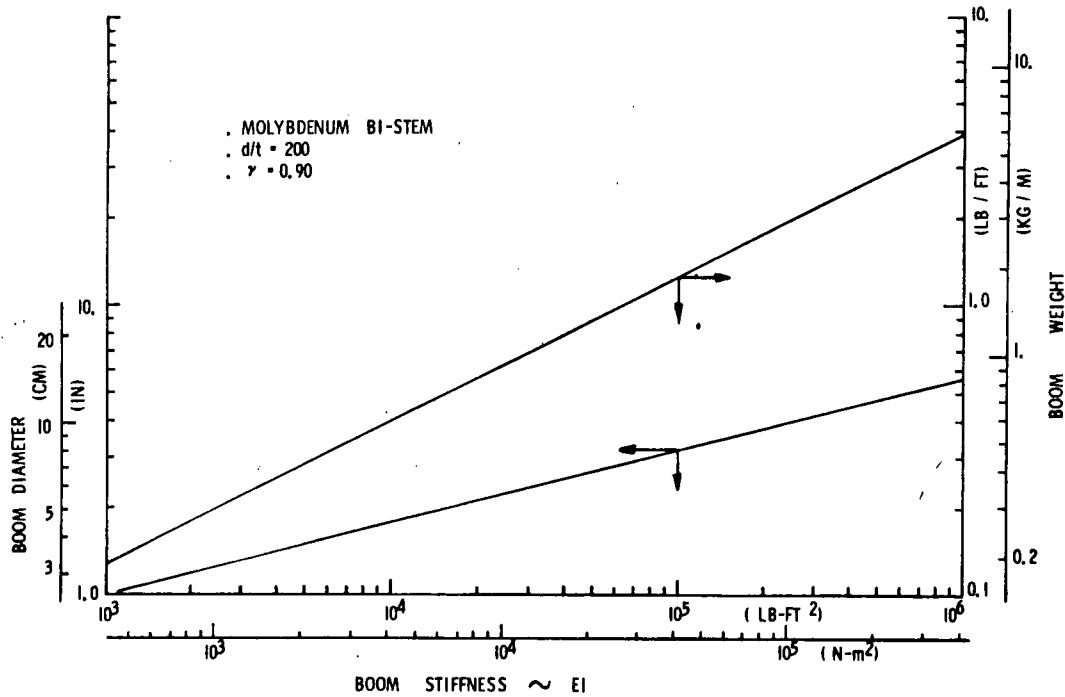


Figure 7. Molybdenum BI-STEM Weight and Diameter as a Function of Bending Stiffness

previous optimization studies (Reference 2).

To verify that the analysis method provided the optimum design, additional analyses were performed which varied the blanket tension while holding all other array properties constant. To bracket the range of configurations analyzed in this study, these analyses were performed for aspect ratios of 2 and 10, and required array minimum frequencies of .02 and 0.2 Hertz. The resulting variations in the symmetric and antisymmetric frequencies with blanket tension are shown in Figures 8 and 9. These curves show that any increase in blanket tension over that required to obtain the desired antisymmetric frequency results in a reduced symmetric frequency, i.e. an increased boom axial load reduces the effective boom stiffness sufficiently to lower the symmetric (bending) frequency of the array. Although a reduction in blanket tension from that required to obtain the required antisymmetric frequency provides a slight increase in the symmetric frequency for the aspect ratio of 2 configuration, the antisymmetric frequency is reduced so that it no longer satisfies the minimum resonant frequency requirement. On the other hand, the aspect ratio of 10 configuration results in a symmetric frequency reduction for tensions other than that which satisfies the antisymmetric frequency requirement. For either configuration, the results of the tension variation analysis confirm that the selected approach results in an optimum design.

For the boron/aluminum BI-STEM (or the continuous longeron ASTROMAST) configuration, Figure 10 shows the optimum boom stiffness and tension as a function of frequency for various values of aspect ratio ( $L'/2w$ ). The baseline design point at an  $L'/2w$  ratio of  $18.565/(2)(2.830) = 3.28$  is shown to have the required frequency of 0.04 Hz with a bending stiffness of  $3447 \text{ N-m}^2$  and a total blanket

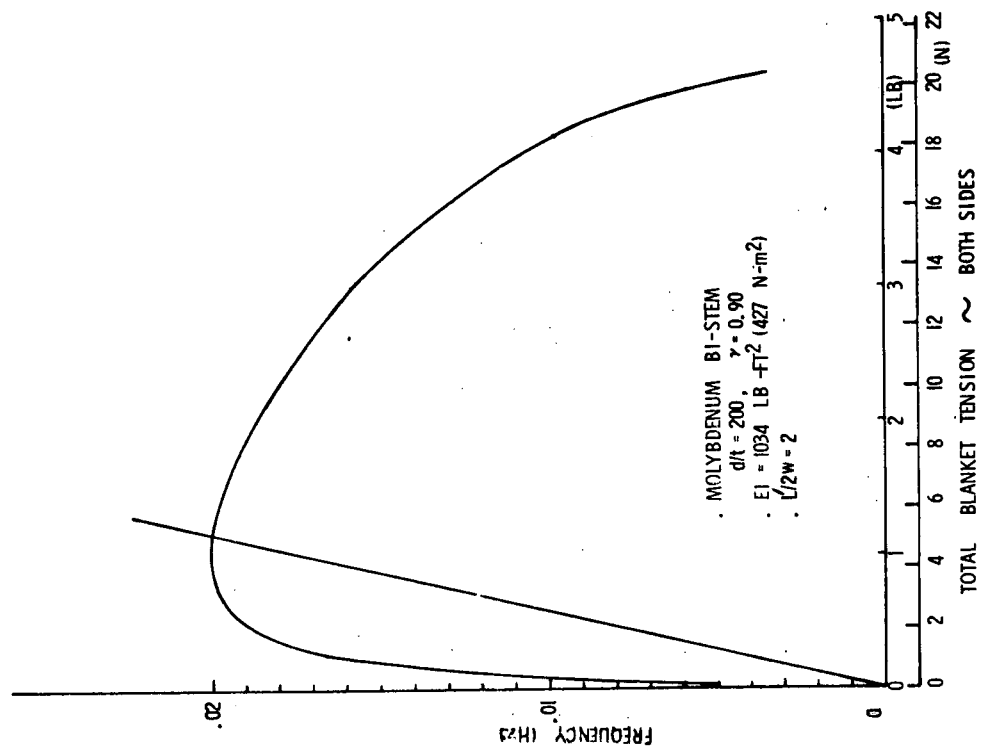


Figure 9. Symmetric and Anti-Symmetric Frequency vs. Tension

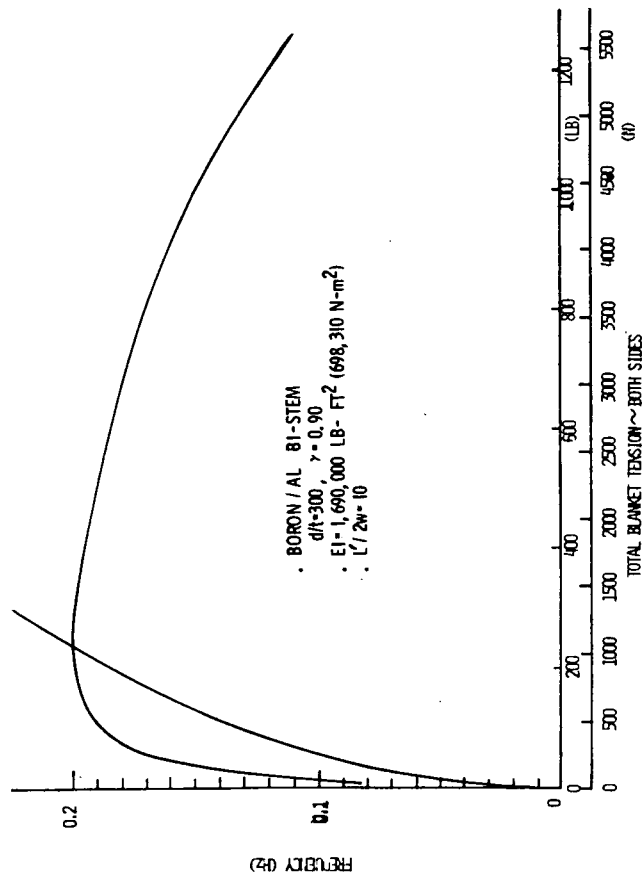


Figure 8. Symmetric and Anti-Symmetric Frequency vs. Tension

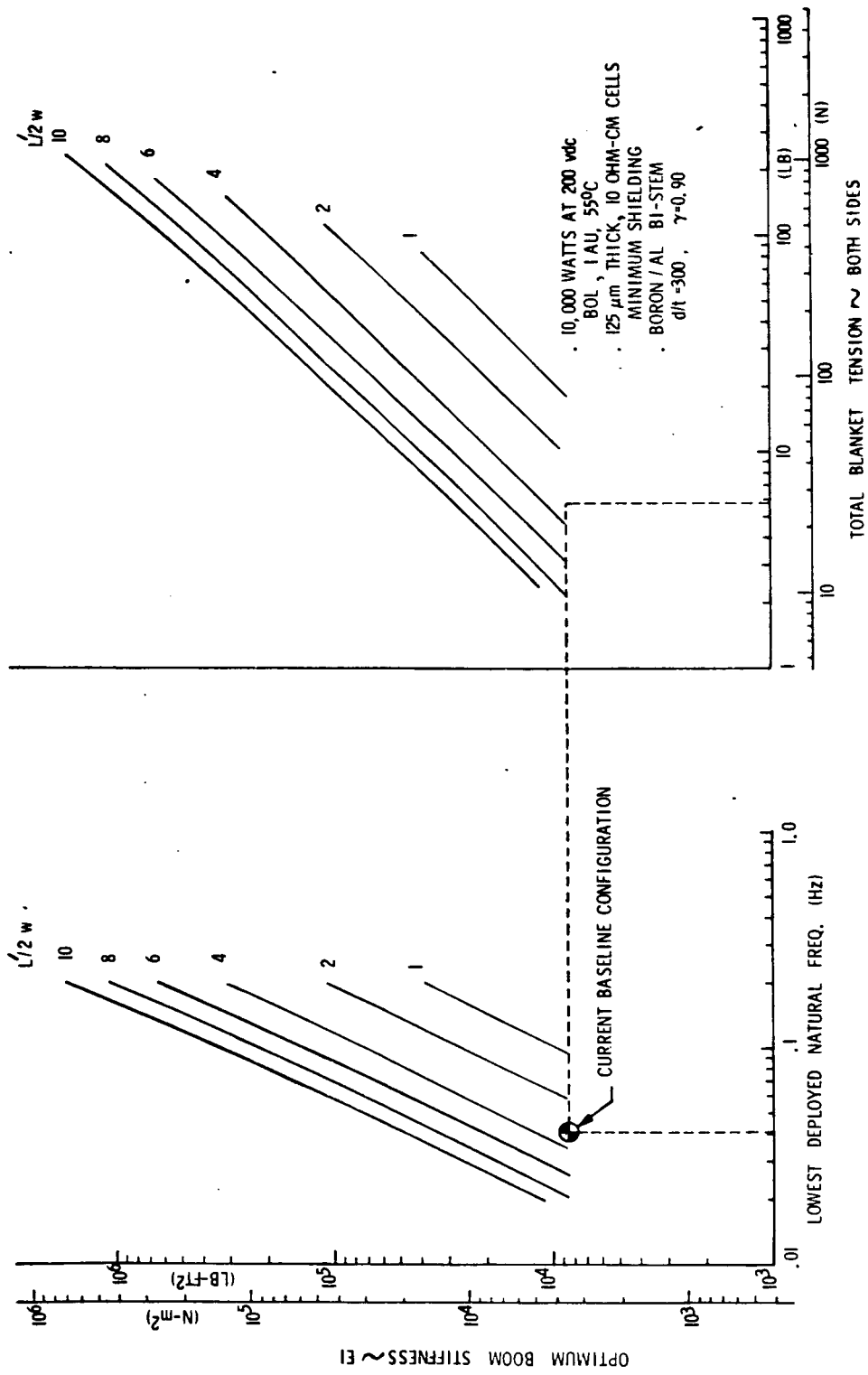


Figure 10. Optimum Boom Stiffness and Tension vs. Frequency

tension (both sides) of 26N. For the molybdenum BI-STEM configuration, a similar presentation of the data are shown in Figure 11.

#### 2.2.1.2 Deployment and Support Structure Analysis

The total system weight consists of the sum of the weights of the three major subsystems: (1) solar cell blankets, (2) deployment structure and mechanisms, and (3) stowage structure and mechanisms. For this analysis, the solar cell blanket weight was assumed to remain constant at 48.5 kg independent of aspect ratio. This simplification ignores the variation of bus strip weight with aspect ratio which could amount to an error of about 3 kg in total blanket weight over the range of aspect ratios considered in this study.

The weight of the deployment structure and mechanisms includes the deployable boom element as well as the actuator required to deploy the element. Figure 6 gives the boom weight and diameter as a function of required boom bending stiffness for a boron/aluminum BI-STEM type element with a d/t ratio of 300. Note that stiffnesses of less than  $3447 \text{ N-m}^2$  are not achievable with this material due to the minimum element thickness restriction of  $178 \mu\text{m}$ . Figure 7 shows the same boom properties for a molybdenum element with a d/t ratio of 200.

The weight of the actuator required to deploy the BI-STEM type elements is given in Figure 12 as a function of boom diameter. This curve is based on limited data for existing BI-STEM designs where the largest size is 5.08 cm in diameter. The comparison of boom types in Section 2.3 shows that the total weight (mast plus canister) of a continuous longeron ASTROMAST is almost identical to the total weight of a boron/aluminum BI-STEM system.



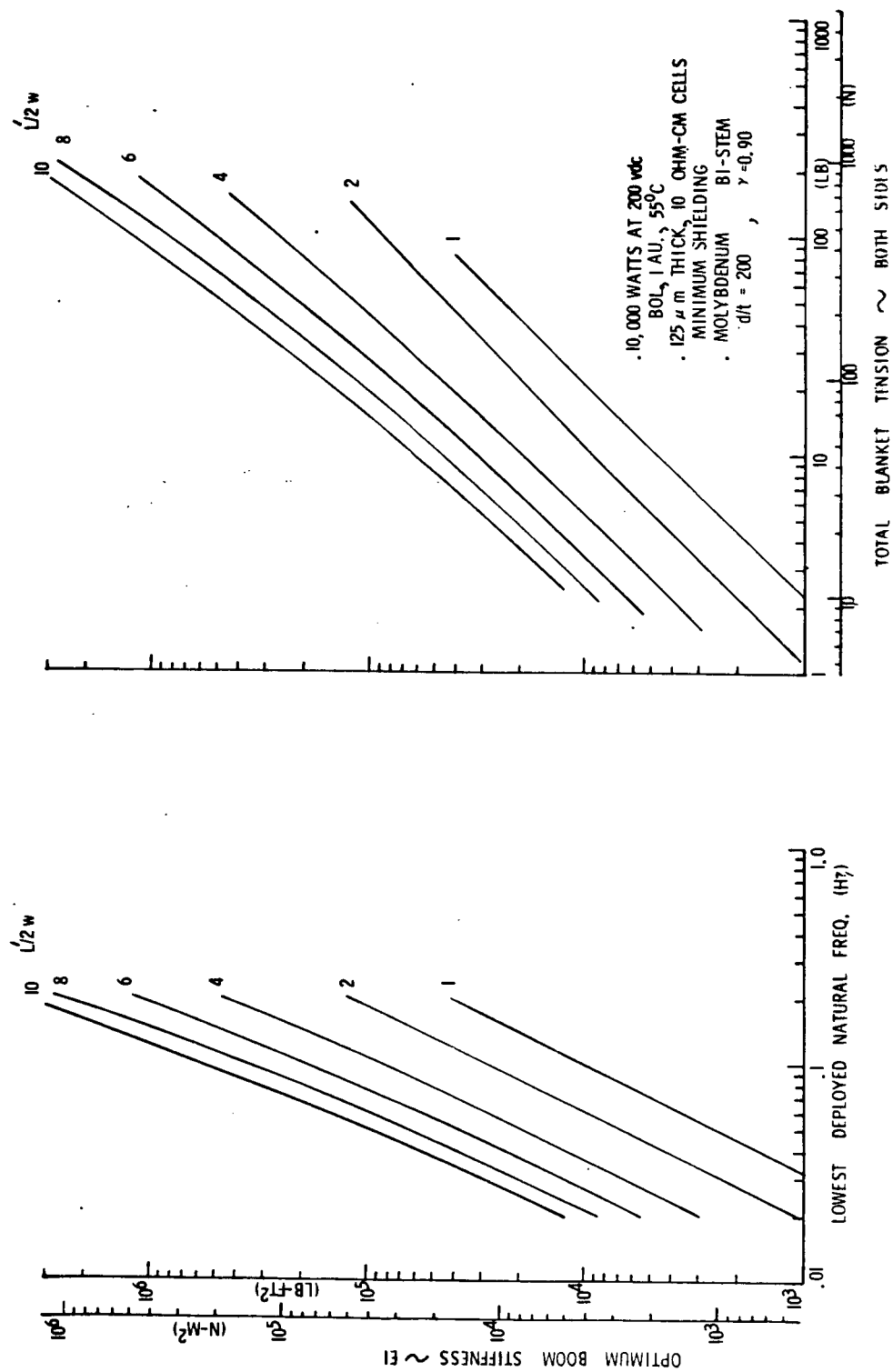


Figure 11. Optimum Boom Stiffness and Tension vs. Frequency

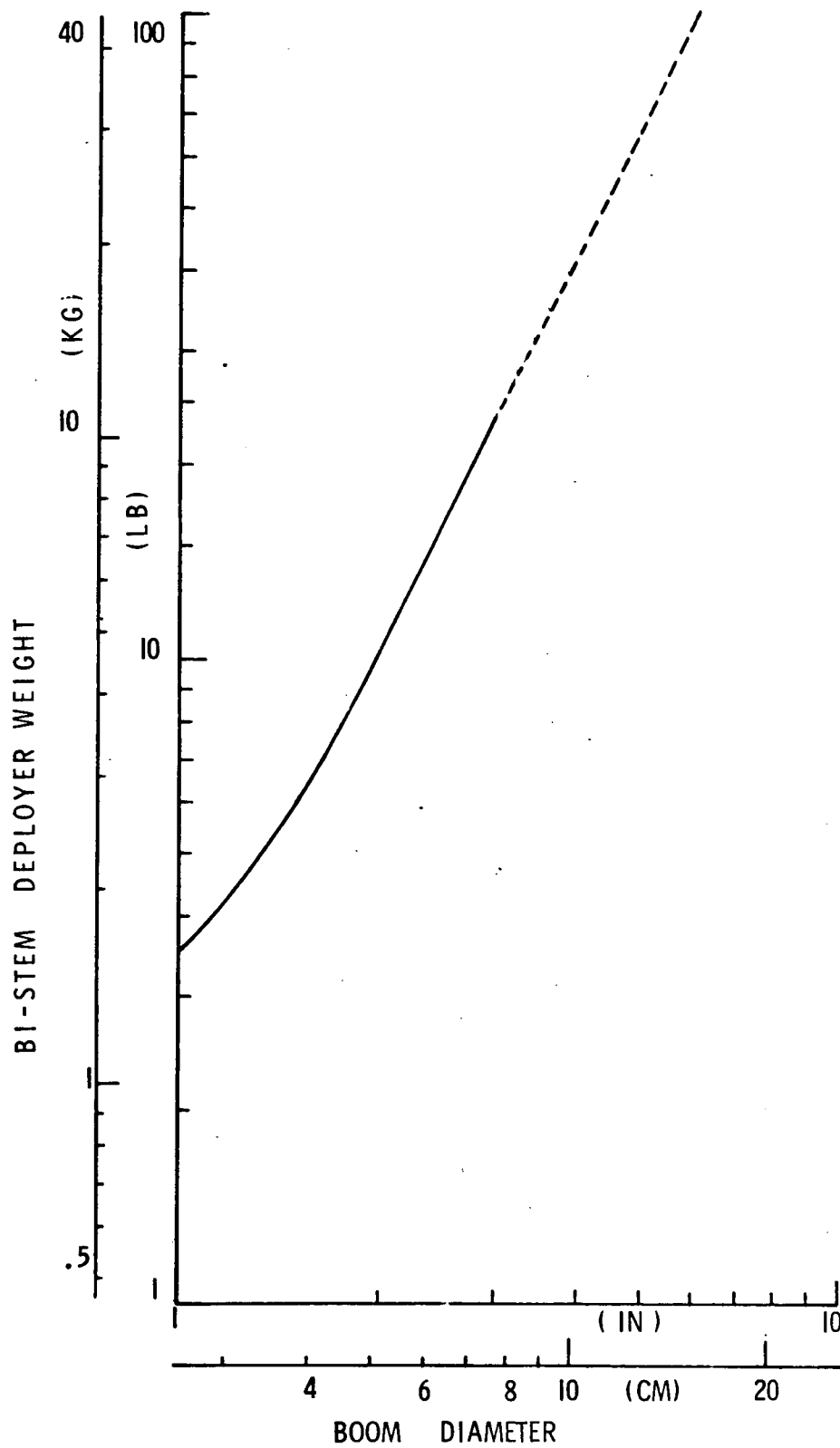


Figure 12. BI-STEM Deployer Weight vs. Boom Diameter

The weight of the stowage structure and mechanisms was calculated based on using the same flat-pack stowage concept as shown in Figure 1 for the current baseline configuration. Figure 13 shows the effects of blanket width,  $w$ , and strip length,  $l$ , on this total structural weight. These curves were established by calculating the weight for the current baseline configuration and proportionately changing the weights as  $w$  and  $l$  were changed. For reasonable changes in these parameters, this proportioning assumption will yield sufficiently accurate weights since most members are sized by minimum gauges and not by stress levels.

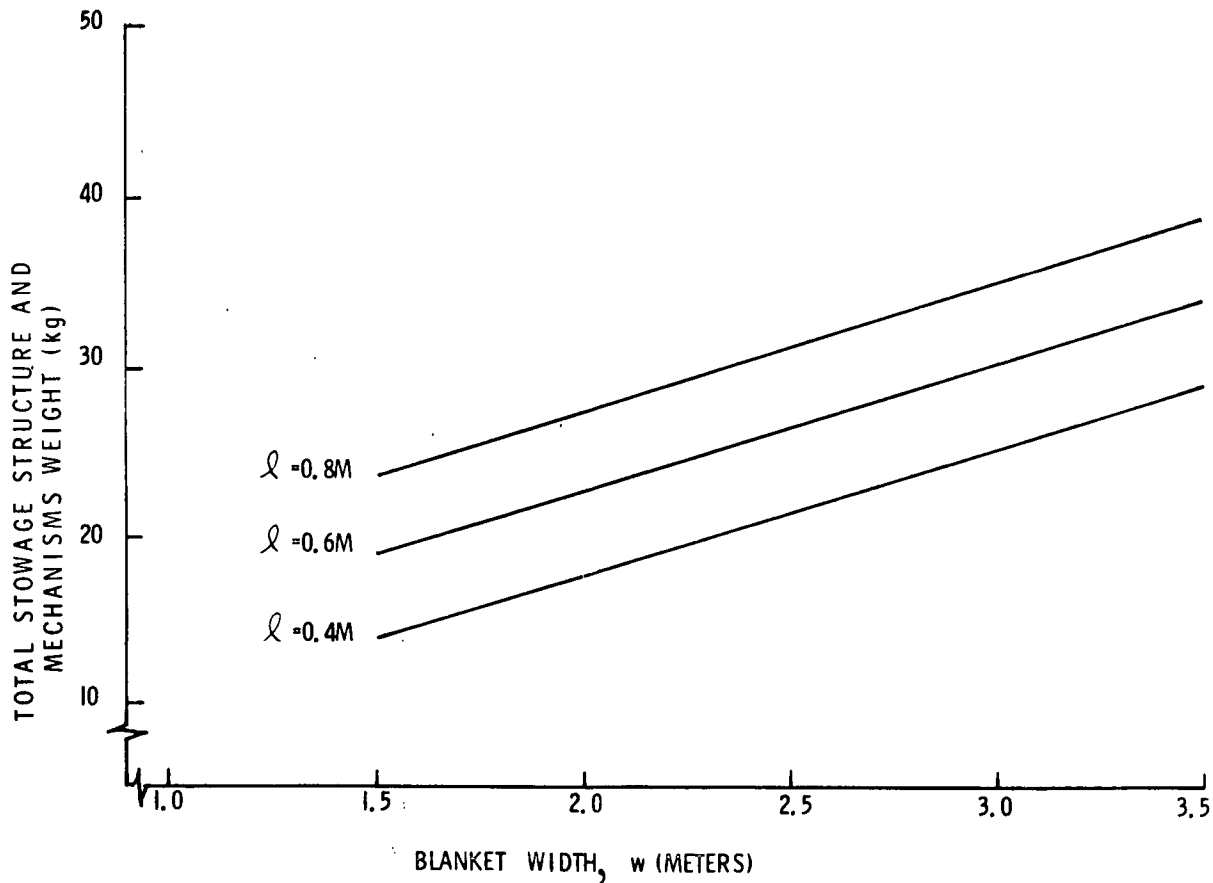


Figure 13. Total Structural Weight vs. Blanket Width and Strip Length

#### 2.2.1.3 Results of Aspect Ratio Study

Based on the previous analyses, it is possible to determine the total array system weight as a function of aspect ratio ( $L'/2w$ ) and deployed natural frequency. Figures 14 and 15 show the total system weight as a function of lowest deployed natural frequency for various values of  $L'/2w$  for the two boom configurations, boron/aluminum and molybdenum, respectively. These same data are plotted in Figures 16 and 17 with aspect ratio on the abscissa. Note that the curves for the boron/aluminum BI-STEM apply equally well for the continuous longeron ASTROMAST since the weight of the mast and canister is virtually identical to an equivalent stiffness B/Al BI-STEM.

### 2.2.2 SOLAR CELL BLANKET CONFIGURATION TRADE-OFFS

#### 2.2.2.1 Introduction

In the preceding section, the total system weight was presented as a function of system blanket aspect ratio. The purpose of this section is to define the allowable blanket geometries in terms of solar cell circuit configurations which meet the electrical requirements. The 10 kw beginning-of-life power output requirement establishes the solar cell area on the blankets for a given selection of solar cell base resistivity and thickness. In addition, the selection of circuit operating voltage has a small effect on total solar cell area since there is an optimum bus strip distribution system power loss which is a function of this voltage (see Reference 1, Section 2.6).

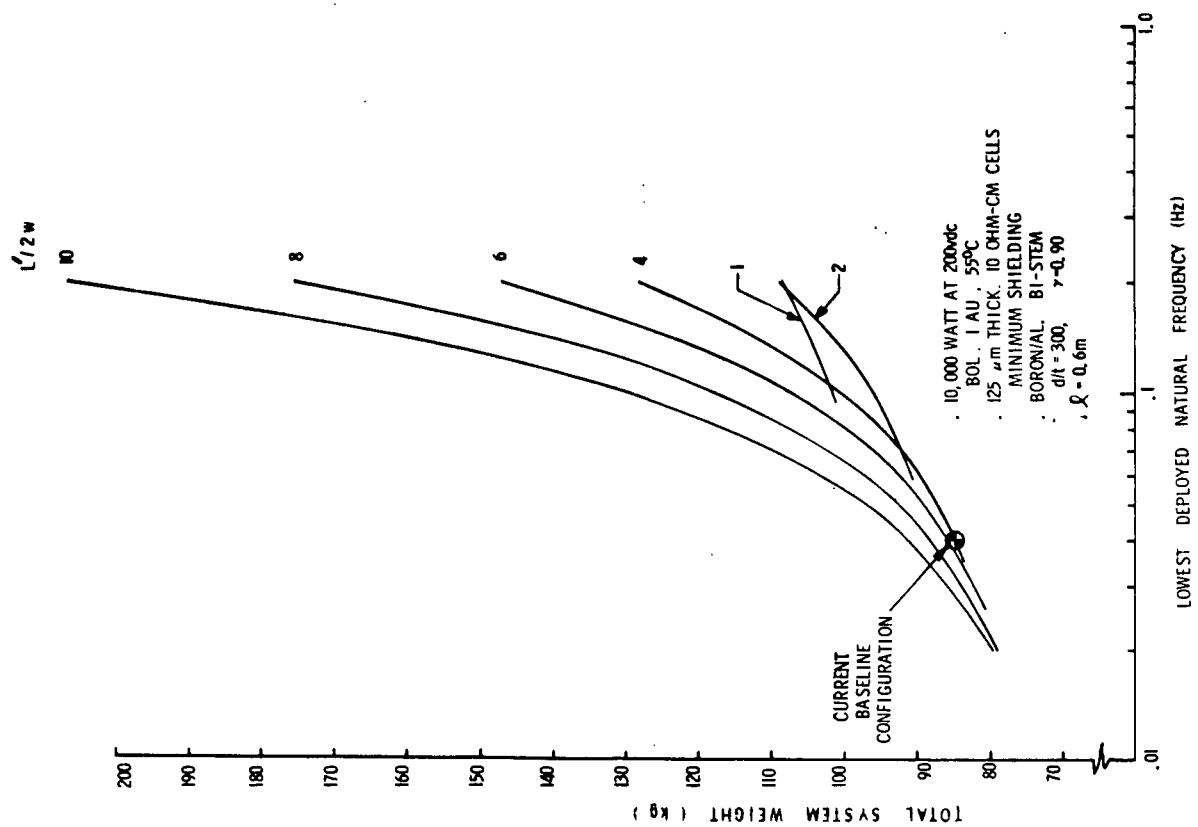


Figure 14. Total System Weight vs.  
Deployed Natural Frequency

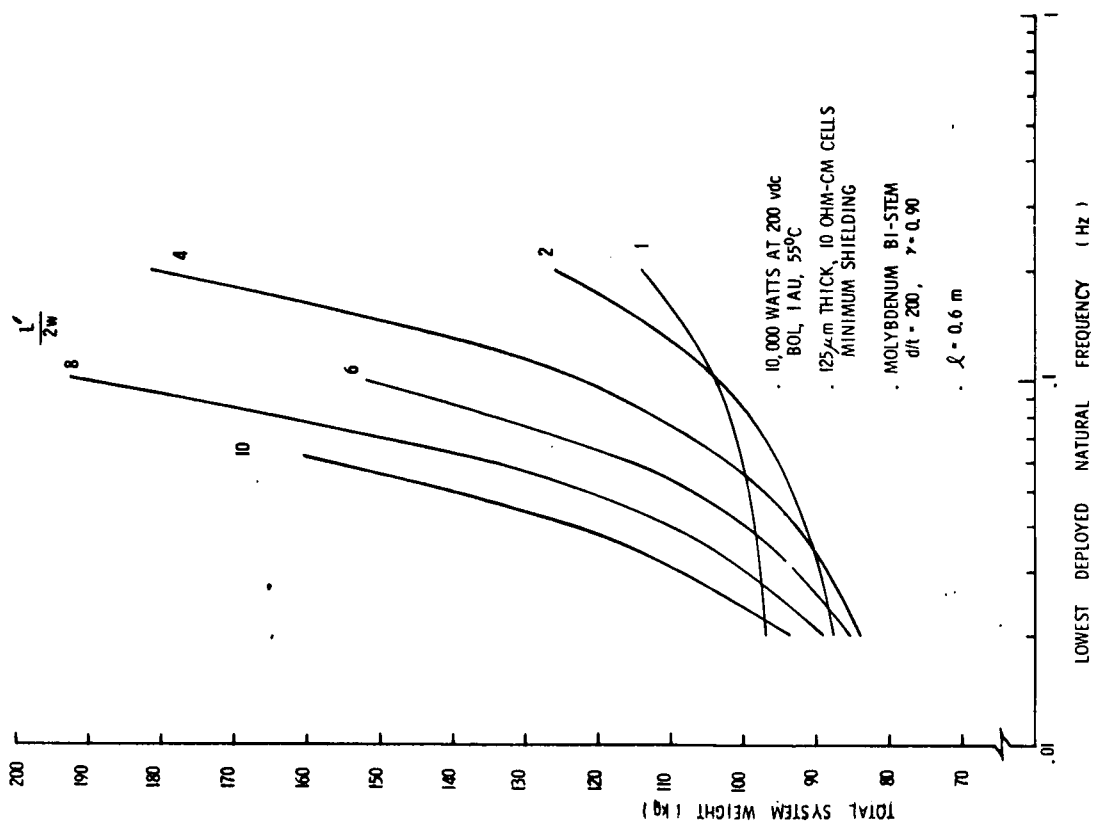


Figure 15. Total System Weight vs.  
Deployed Natural Frequency

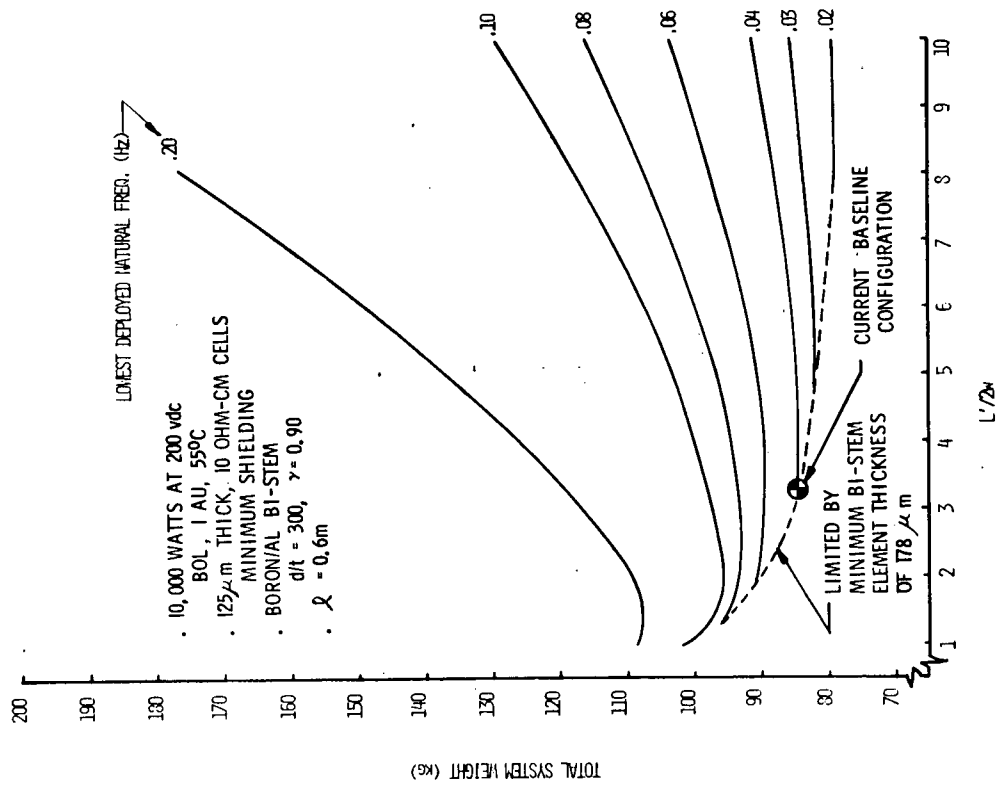


Figure 16. Total System Weight vs. Aspect Ratio

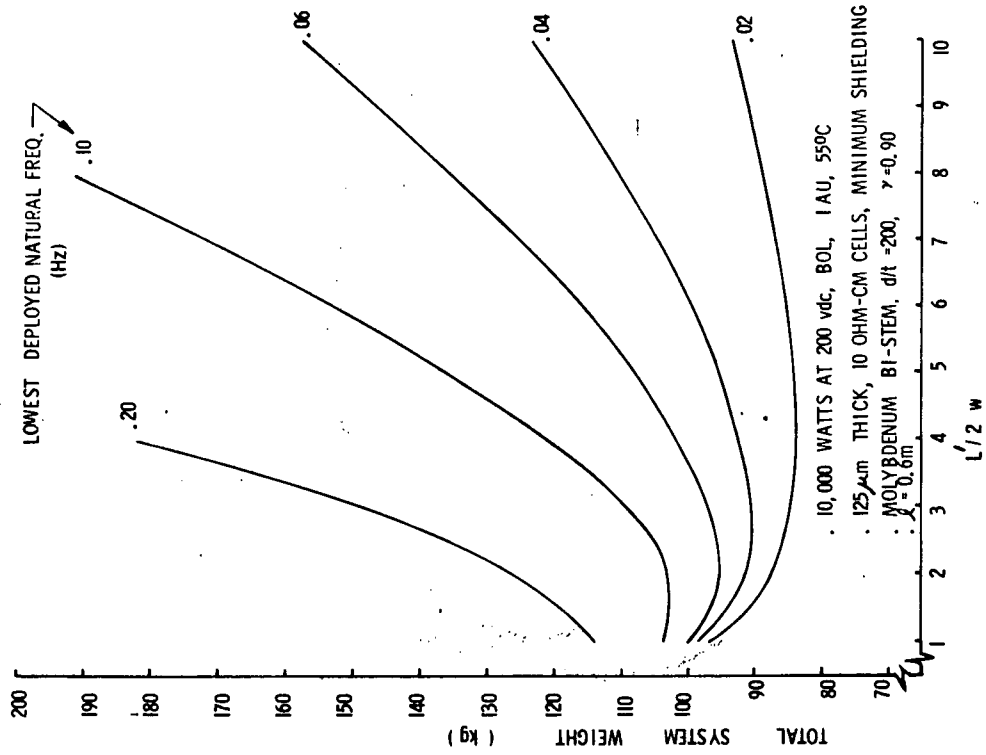


Figure 17. Total System Weight vs. Aspect Ratio

### 2.2.2.2 Definitions and Nomenclature

The basic circuit configuration to be considered is shown in Figure 18. In this context, a circuit is defined as a group of interconnect solar cells which supply power to the solar array bus at the full rated voltage. The solar array consists of a number of identical parallel connected circuits. Each circuit consists of a number of series connected modules. The length of the modules,  $b$ , is the width of the circuit as shown in Figure 18. In turn, each module is composed of a number of series connected submodules which are a parallel connection of solar cells which develop the full module short-circuit current, but only the voltage associated with a single cell. The following list of symbols and definitions will be used in connection with this description:

$N_{P/M}$	=	number of parallel cells per module (or circuit)
$N_{S/C}$	=	number of series cells per circuit
$N_{S/M}$	=	number of series cells per module
$N_{M/C}$	=	number of modules per circuit
$N_{C/B}$	=	number of circuits per blanket
$N_{B/A}$	=	number of blankets per array
$N_{SC/A}$	=	number of solar cells per array
$N_{SC/B}$	=	number of solar cells per blanket
$N_{P/B}$	=	number of parallel cells per blanket

Based on these definitions, the following relations are apparent:

$$\begin{aligned} N_{SC/A} &= N_{SC/B} N_{B/A} \\ N_{SC/B} &= N_{S/C} N_{P/B} \\ N_{SC/B} &= N_{S/C} N_{P/M} N_{C/B} \\ N_{S/C} &= N_{M/C} N_{S/M} \end{aligned} \quad [1]$$

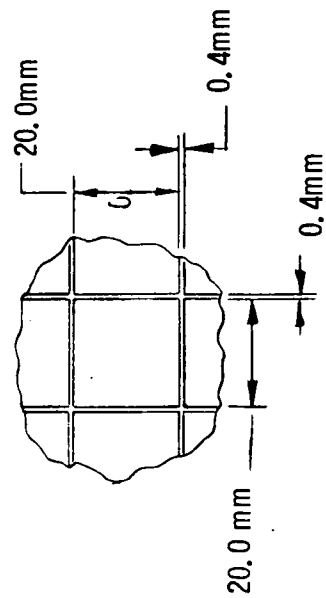
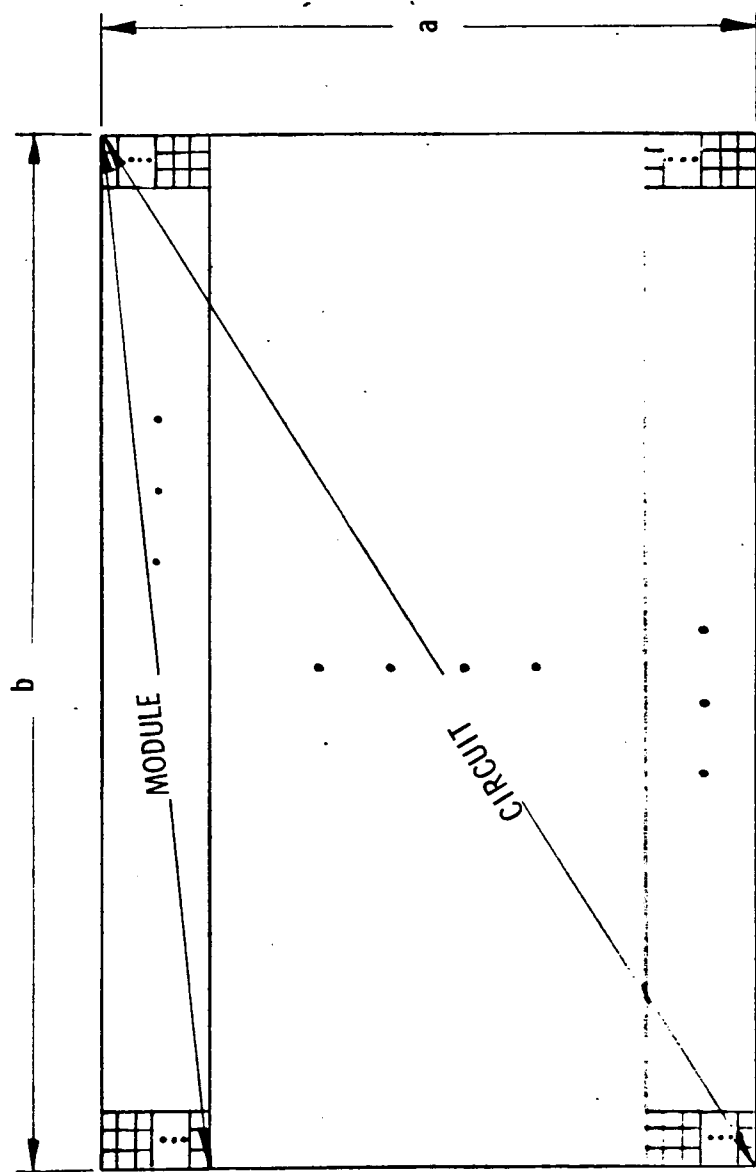


Figure 18. Solar Cell Circuit Configuration



The dimensions of the circuit, a and b, in meters, are given by:

$$\begin{aligned} a &= .0200 N_{P/M} N_{M/C} + .0004 (N_{P/M} N_{M/C} - 1) \\ b &= .0200 N_{S/M} + .0004 (N_{S/M} - 1) \end{aligned} \quad [2]$$

Figure 19 shows the arrangements of circuits on a blanket. The module length, b, has been placed normal to the deployment direction of the solar array. The blanket width, w, is larger than b by the amount required to accommodate the bus strips on both sides. A strip, as shown on the figure, represents a separable portion of a blanket. In other words, the blanket is composed of the series mechanical connection of a number of strips. A strip may or may not contain a complete electrical circuit. Thus, the strip length, a', may or may not be equal to the circuit length, a on Figure 18. For a flat pack stowage concept, the blanket is folded at each space between strips. The length of the blanket, L, is given by:

$$L = a' N_{ST/B} + s(N_{ST/B} - 1) \quad [3]$$

where

$N_{ST/B}$  = number of strips per blanket

s = separation required between strips to accommodate fold.

Note that this length, L, does not include either an inboard or outboard leader length.

### 2.2.2.3 Candidate Blanket Configurations

With a nominal 125  $\mu\text{m}$  thick, 10 ohm-cm solar cell, the maximum power voltage is 0.375 volts per cell at 55°C. Assuming a 1-percent voltage loss within the modules, 540 series connected cells are required to provide a 200 volt system bus voltage. The 540 series connected cell circuit arrangement is convenient because

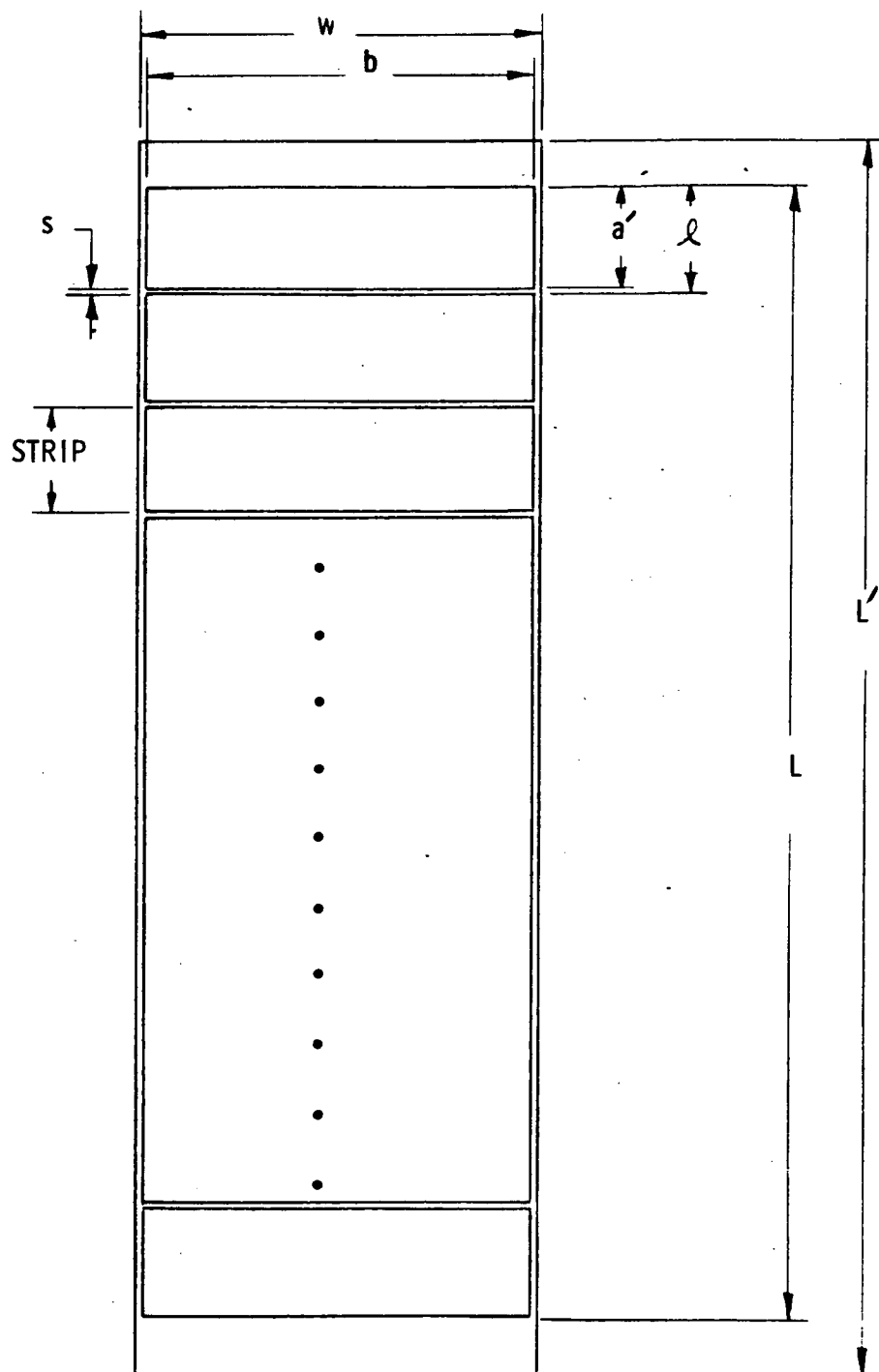


Figure 19. Solar Cell Blanket Configuration

it allows for a wide choice of module lengths since the number 540 is evenly divisible by 2, 3, 4, 5, 6, 9, etc. Table 6 shows the possible module lengths and module maximum power voltage for 10 ohm-cm cells operating at 55°C.

Table 6. Possible Module Lengths

$N_{S/M}$	Module Maximum Power Voltage for 10 ohm-cm Cells Operating at 55°C (volts)	b (m)
540	200	11.0156
270	100	5.5076
180	66.7	3.6716
135	50	2.7536
108	40	2.2028
90	33.3	1.8356
60	22.2	1.2236
54	20	1.1012
45	16.7	0.9176
36	13.3	0.7340
30	11.1	0.6116
27	10	0.5504

For a total solar array power output of 10,000 watts at beginning-of-life, the number of solar cells required is given by:

$$N_{SC/A} = N_{S/C} N_{P/B} N_{B/A} = \frac{10,000}{P_{cell} (1 - \alpha_o)(1 - \gamma)} \quad [4]$$

where  $P_{cell}$  = cell maximum power output at 55°C, 1 A.U.  
= .0464 watts for 125  $\mu$ m thick 10 ohm-cm cells  
= .0442 watts for 100  $\mu$ m thick 10 ohm-cm cells  
 $\alpha_o$  = optimum bus strip power loss from Figure 53 of Reference 1  
= .02 for  $V = 200$  volts, a blanket aspect ratio of 10, and 10 circuits per blanket  
 $\gamma$  = module assembly power loss, including interconnector series resistance and current mismatch  
= .03

Therefore,  $N_{P/B} N_{B/A} = 420$  for the 125  $\mu\text{m}$  thick cells and 442 for the 100  $\mu\text{m}$  thickness, or for a two blanket per solar array system, the number of required parallel solar cells per blanket,  $N_{P/B}$ , is 210 and 221, respectively. For the manned space station mission where the use of 2 ohm-cm cell base resistivity is indicated (see Reference 1, Section 2.5), and the design operating temperature is about 80°C, the direct substitution of 2 ohm-cm cells for 10 ohm-cm cells in the same circuit configuration will yield a slightly greater output (<1%) at the same maximum power voltage. This is demonstrated by the data plotted in Figure 20 which show that the 2 ohm-cm cells operating at 80°C have almost exactly the same maximum power point as 10 ohm-cm cells operating at 55°C.

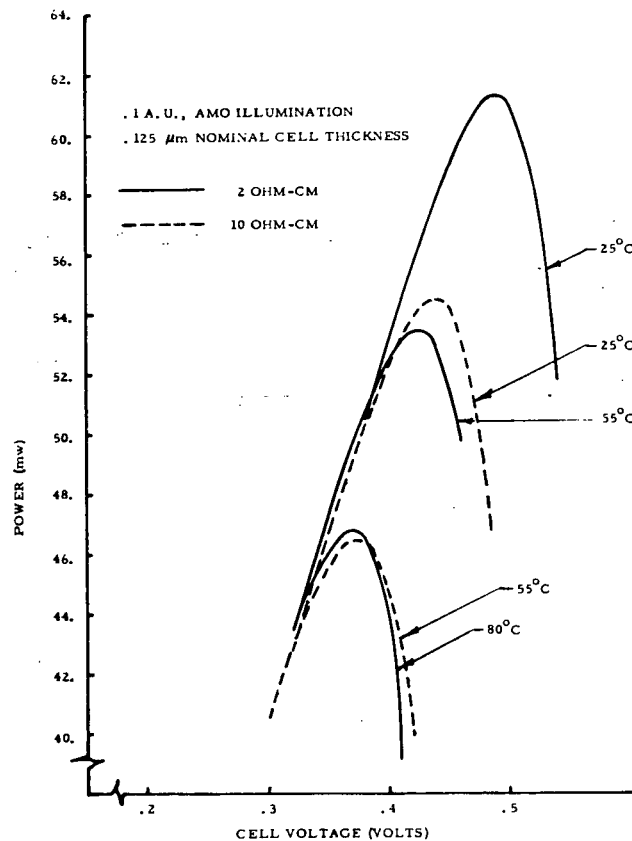


Figure 20. Comparison of 2 and 10 ohm-cm Cells at Various Operating Temperatures

Table 7 lists the possible circuit arrangements for  $N_{S/C} = 540$  and  $N_{P/M} N_{C/B} = 210$  and 221. From among these possible combinations of  $N_{P/M}$  and  $N_{C/B}$ , the most practical choices have been indicated by a box in the table. For each of these most practical circuit arrangements, it is possible to establish the associated configurations of the blanket based on the definition of terms from Figure 19.

Table 7. Possible Circuit Arrangements for  $N_{S/C} = 540$

$N_{P/M} N_{C/B}$	210		221	
$N_{S/C/A}$	226,800		238,680	
	$N_{P/M}$	$N_{C/B}$	$N_{P/M}$	$N_{C/B}$
	1	210	1	221
	2	105	13	17
	3	70	17	13
	5	42	221	1
	6	34		
	7	30		
	10	21		
	14	15		
	15	14		
	21	10		
	30	7		
	35	6		
	42	5		
	70	3		
	105	2		
	210	1		

Table 8 lists the possible blanket configurations for  $N_{P/M} N_{C/B} = 221$ . The strip length,  $a'$ , has been limited to about 1 meter to allow for convenient handling of individual strips. Thus, if the circuit length,  $a$  from Figure 18, exceeds about 1 meter, the circuit is divided between two or more strips. For example, in row 4 of Table 8, the six module electrical circuit has been divided between two strips to limit the strip length. The total blanket length, as given by equation [3], is tabulated for three values of  $s$ , the separation between strips. The corresponding blanket area, for one of the two blankets, and the ratio,  $L/b$ ,

Table 8. Possible Blanket Configurations for  $N_{P/M} N_{C/B} = 221$

$N_{P/M}$	$N_{C/B}$	$N_{M/C}$	(1) $N_{M/ST}$	(2) $N_{ST/B}$	$b$ (m)	$a'$ (m)	$L$ (m)			Blanket Area (m <sup>2</sup> )			$L/b$		
							$s=3$ cm	$s=4$ cm	$s=5$ cm	$s=3$ cm	$s=4$ cm	$s=5$ cm	$s=3$ cm	$s=4$ cm	$s=5$ cm
13	17	2	2	17	5.5076	0.5300	9.4900	9.6500	9.8100	52.2671	53.1483	54.0296	1.7230	1.7521	1.7812
		3	3	17	3.6716	0.7952	13.9984	14.1584	14.3184	51.3965	51.9840	52.5714	3.8126	3.8562	3.8998
		4	4	17	2.7536	1.0604	18.5068	18.6668	18.8268	50.9603	51.4009	51.8415	6.7209	6.7791	6.8372
		6	3	34	1.8356	0.7952	28.0268	28.3568	28.6868	51.4460	52.0517	52.6575	15.2684	15.4482	15.6280
		9	3	51	1.2236	0.7952	42.0552	42.5552	43.0552	51.4587	52.0705	52.6823	34.3700	34.7787	35.1873
17	13	2	2	13	5.5076	0.6932	9.3716	9.4916	9.6116	51.6150	52.2759	52.9368	1.7015	1.7234	1.7452
		3	3	13	3.6716	1.0400	13.8800	14.0000	14.1200	50.9618	51.4024	51.8430	3.7803	3.8131	3.8457
		4	2	26	2.7536	0.6932	18.7732	19.0232	19.2732	51.6939	52.3823	53.0707	6.8176	6.9085	6.9993
		6	3	26	1.8356	1.0400	27.7900	28.0400	28.2900	51.0113	51.4702	51.9291	15.1394	15.2757	15.4119
		9	3	39	1.2236	1.0400	41.7000	42.0800	42.4600	51.0241	51.4891	51.9541	34.0797	34.3903	34.7009

NOTES: (1) number of modules per strip.  
(2) number of strips per blanket

are given for the same three values of  $s$ .

A similar tabulation for  $N_{P/M} N_{C/B} = 210$  is given in Table 9 for a value of  $s = 3$  cm. The selected circuit arrangement and corresponding blanket configuration for the current baseline configuration have been indicated in this table.

### 2.3 COMPARISON OF DEPLOYABLE BOOM TYPES

A comparison of the BI-STEM deployable boom type with a continuous longeron coilable lattice ASTROMAST was performed to determine the total weight of each system over the range of bending stiffnesses of interest on this program. These results are shown on Figure 21 for a BI-STEM type boom which is fabricated from three different materials: stainless steel, molybdenum, and 50 v/o boron/aluminum composite. The boom length, in all cases, is 18.29 m (60 ft) and the total weight

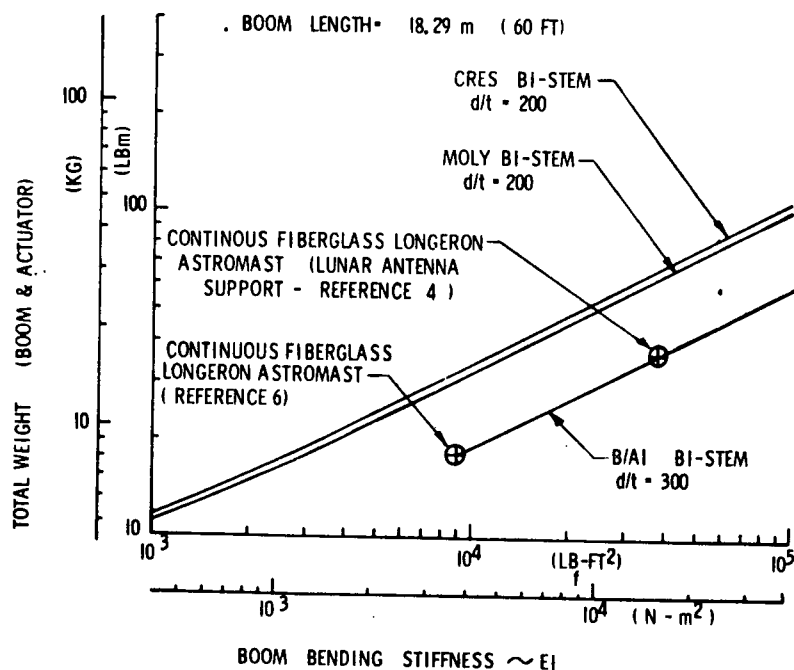


Figure 21. Comparison of Deployable Boom Types

Table 9. Possible Blanket Configurations for  $N_{P/M} N_{C/B} = 210$  (with  $S = 3$  cm)

$N_{P/M}$	$N_{C/B}$	$N_{M/C}$	$N_{M/ST}$	$N_{ST/B}$	$b$ (m)	$a'$ (m)	$L$ (m)	Blanket Area (m <sup>2</sup> )	$L/b$
10	21	2	2	21	5.5076	.4076	9.1596	50.4474	1.6630
		3	3	21	3.6716	.6116	13.4436	49.3395	3.6615
		4	4	21	2.7536	.8156	17.7276	48.8147	6.4379
		5	5	21	2.2028	1.0196	22.0116	48.4872	9.9925
		6	3	42	1.8356	.6116	26.9172	49.4092	14.6639
		9	3	63	1.2236	.6116	40.3908	49.4222	33.0098
		10	5	42	1.1012	1.0196	44.0532	48.5114	40.0047
		2	2	15	5.5076	.5708	8.9820	49.4693	1.6308
		3	3	15	3.6716	.8564	13.2660	48.7074	3.6131
		4	2	30	2.7536	.5708	17.9940	49.5483	6.5347
14	15	6	3	30	1.8356	.8564	26.5620	48.7572	14.4705
		9	3	45	1.2236	.8564	39.8580	48.7702	32.5744
		2	2	14	5.5076	.6116	8.9524	49.3062	1.6255
		3	3	14	3.6716	.9176	13.2364	48.5988	3.6051
		4	2	28	2.7536	.6116	17.9348	49.3853	6.5132
		6	3	28	1.8356	.9176	26.5028	48.6485	14.4382
		9	3	42	1.2236	.9176	39.7692	48.6616	32.5018
		2	2	10	5.5076	.8564	8.8340	48.6541	1.6040
		4	2	20	2.7536	.8564	17.6980	48.7332	6.4272
		6	2	30	1.8356	.8564	26.5620	48.7572	14.4705
21	10	10	2	50	1.1012	.8564	44.2900	48.7721	40.2198

Current  
Baseline  
Configu-  
ration



includes both the boom and the actuator (or deployer). The continuous longeron coilable lattice ASTROMAST is represented by one point at a bending stiffness of  $1.58 \times 10^4 \text{ N-m}^2$  ( $3.82 \times 10^4 \text{ lb-ft}^2$ ) which corresponds to a 25.4 cm (10 inch) diameter antenna support mast for use on the lunar surface and by another point at a bending stiffness of  $3.72 \times 10^3 \text{ N-m}^2$  ( $9.0 \times 10^3 \text{ lb-ft}^2$ ) which corresponds to a 17.8 cm (7 inch) diameter mast. The 25.4 cm (10 inch) diameter unit is 30.48 m (100 ft) long and weighs a total of 22.68 kg (50 lb) which is distributed as 9.07 kg (20 lb) for the mast and 13.61 kg (30 lb) for the canister or deployer (Reference 4). The total reflected by this point on Figure 21 has been scaled-down, using the technique described in Reference 5, to account for the reduced length. The weight of the 17.8 cm (7 inch) diameter mast was obtained from Reference 6.

Based on these comparison points, it can be concluded that the fiberglass continuous longeron coilable lattice ASTROMAST is superior, from a weight standpoint, to a BI-STEM type boom which uses conventional metallic elements (viz., CRES or molybdenum). The boron/aluminum BI-STEM element, which is discussed in Section 2.5.2, is weight competitive with the continuous longeron ASTROMAST, but represents an advancement in the state-of-the-art. The only other major difference between the continuous longeron ASTROMAST and the boron/aluminum BI-STEM is in the size of the deployer required. For a bending stiffness of  $3.72 \times 10^3 \text{ N-m}^2$  ( $9.0 \times 10^3 \text{ lb-ft}^2$ ), the ASTROMAST canister will be about 86 cm (34 inches) high by 23 cm (9 inches) in diameter while the BI-STEM actuator will be about 36 cm (14.2 inches) high by 20 cm (7.9 inches) wide by 24 cm (9.5 inches) deep. The considerably longer height in the deployment direction makes the integration of the ASTROMAST into the overall system more difficult. The use of a lanyard deployment scheme with the continuous longeron ASTROMAST will eliminate the function

of the motor driven deployment canister and reduce the stowed height of the mast to about 53 cm (21 inches). The loads on the mast during deployment must be evaluated to determine if such a lanyard deployment concept can be used.

## 2.4 ANALYSIS OF A "V"-STIFFENED SOLAR ARRAY

### 2.4.1 INTRODUCTION

A "V" stiffened solar array configuration has been conceived as a means of obtaining significant increases in the minimum array resonant frequency without added complexity. Thus it is possible to meet a specified deployed natural frequency requirement with reduced boom stiffness (and reduced total system weight) when compared with a planar array geometry. This concept, shown in Figure 22, uses the slight angle of the array blankets to enable observed in-plane stiffening

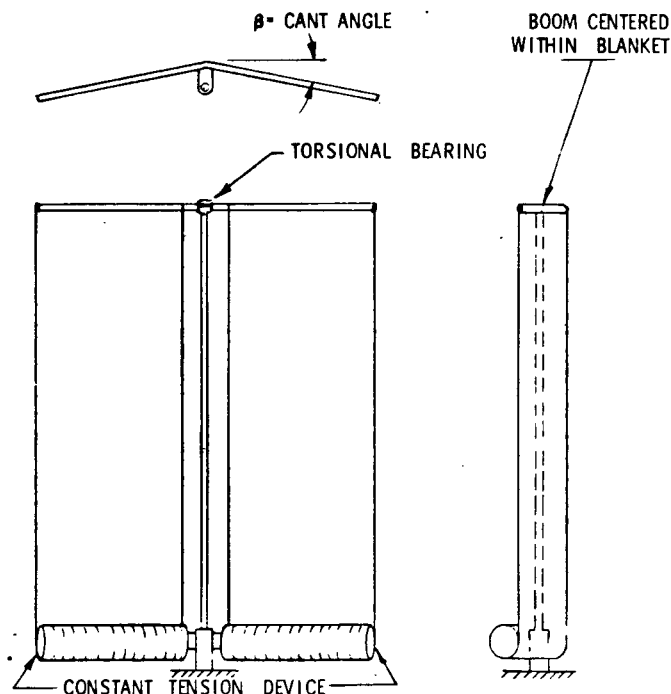


Figure 22. "V" Configuration, Single Boom Solar Array Concept

resulting from the redistribution of blanket tension to provide out-of-plane stiffness. Static tests and analysis of the RA250 in-plane behavior (Reference 7) showed that the array blanket tension was redistributed such that the array rotated about one edge. In effect, the blanket provided a moment constraint to the tip of the deployable boom until an edge tension condition was achieved after which the boom behaved as a cantilever. By canting the blankets and centering the boom within the blankets, this boom tip constraint can also be used to stiffen the array for symmetric out-of-plane motion.

The effect of the canted blankets will also provide stiffening for torsional motion of the array. For a given boom, the tip constraint will enable greater tension to be applied without buckling the boom; hence, an increase in the torsional frequency. In addition, the boom will be required to bend during torsional vibration with some increase in the frequency. (Because of the high in-plane stiffness, the array will tend to twist about the center of the "V" causing bending of the boom.) However, this analysis is only concerned with the effects of the canted blankets on the symmetric frequency; torsional stiffening should be considered in a subsequent analysis.

The approach used in the analysis is to use the present out-of-plane analytical model of the array with linear modifications to the boom stiffness which account for the effect of the canted blankets at various amplitudes of motion. The first portion of this section reviews the in-plane analysis and test results for the RA250 which are used for modifying the boom stiffness. The symmetric analysis of the "V" Stiffened Array is then presented. Effects of the "V" configuration on the "baseline" array are then discussed.

#### 2.4.2 RA250 IN-PLANE TEST AND ANALYSIS

The study of the in-plane behavior of the RA250 (Reference 7) showed that the shift in the blanket tension distribution was a major factor in the observed stiffness. The tests indicated that there were three regions of different stiffnesses for in-plane deflections as shown in Figure 23 and described below:

Region 1: For small deflections, hysteretic behavior of the BI-STEM boom caused a relatively high stiffness. This is best predicted semi-empirically and is not predicted by simplified analytical modeling.

Region 2: For medium deflections, the tension distribution of the blankets changes such that the slope ( $\Theta$ ) at the tip of the boom (Leading Edge Member) is proportional to the tip deflection ( $\delta$ ) divided by the array length (L).

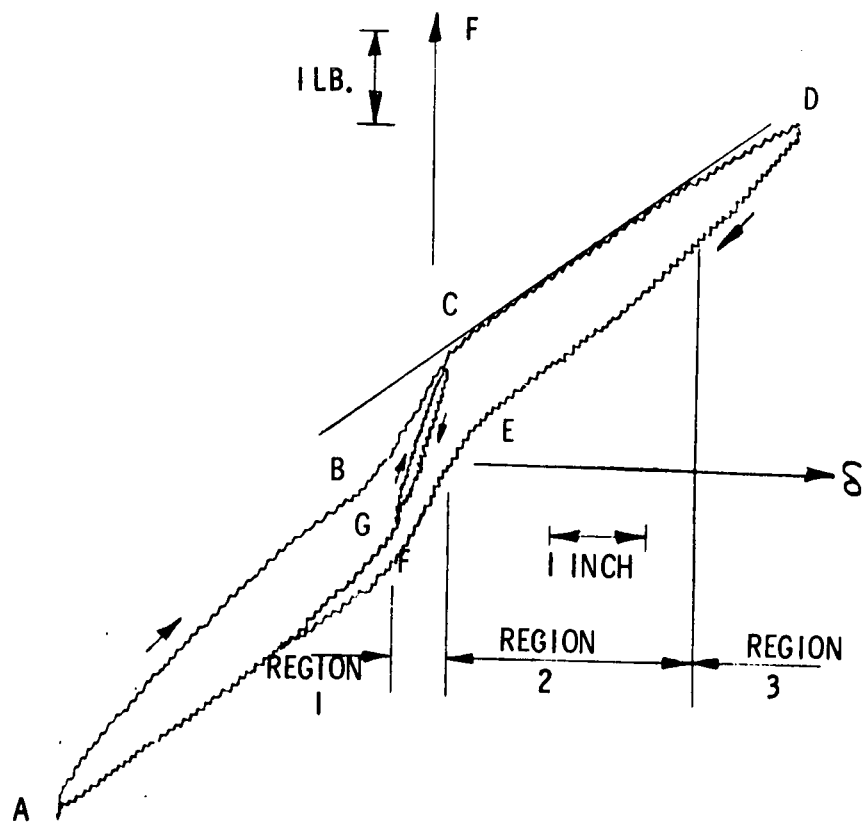
$$\Theta = \delta/L \quad [5]$$

This results from a constraining moment at the tip of the boom due to the blanket tension and is valid until the tension shifts to the edges of the blanket. The deflection at which this region ends is represented by

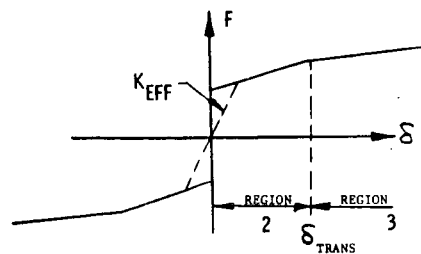
$$\delta_{\text{TRANS}} = Tw \left[ \frac{2 EI}{L^2 (1 + 4 \bar{\alpha})} + \frac{T(1 + 12 \bar{\alpha})}{15(1 + 4 \bar{\alpha})^2} \right]^{-1} \quad [6]$$

where

T	=	Tension per blanket
EI	=	Boom stiffness
$\bar{\alpha}$	=	Factor accounting for root flexibility
	=	$EI/K_r L$
w	=	Half width of the array



(a) Measured on RA250 (From Reference 7)



(b) Linearized

Figure 23. In-Plane Force-Deflection Characteristic

In Region 2, the force deflection characteristic is best represented as:

$$F = \left[ \frac{4 EI}{L^3 (1 + 4 \bar{\alpha})} - \frac{4T}{15 (1 + 4 \bar{\alpha})^2 L} \right] \delta + \frac{T_w}{L} \quad [7]$$

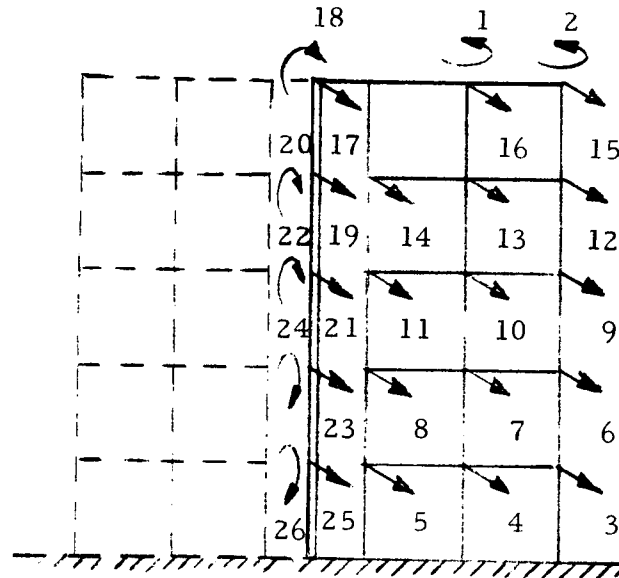
This relation has been shown to provide excellent agreement with RA250 model test results.

Region 3: For large deflections, the effect of blanket tension is no longer present and the boom behaves as a cantilever. This occurs after the transitional deflection given by Equation [6].

Using the idealized representation shown in Figure 23(b), an effective linear stiffness ( $K_{eff}$ ) can be defined for a selected amplitude of motion. Although other methods could be used to arrive at a linearized stiffness, this appears to be a reasonable estimate. It is conservative for large amplitudes in that the stiffness is higher than predicted, but may be unconservative for small amplitudes because the Region 1 stiffness is not included in the stiffness representation.

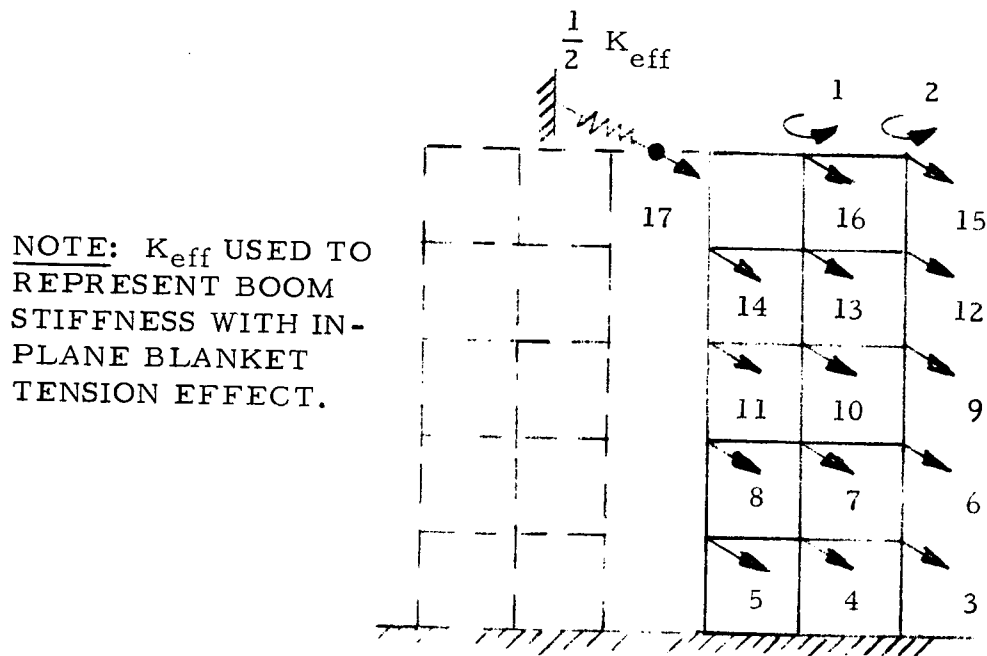
#### 2.4.3 SYMMETRIC VIBRATION ANALYSIS

The approach used in performing this symmetric vibration analysis of the "V" stiffened array was to use the existing model of the blankets and revise the boom stiffness representation to reflect the effect of the blanket tension redistribution. The original analytical model of the array is shown in Figure 24a. The revised model of the array is shown in Figure 24b where the major modification is to replace the boom finite element model by an effective linear spring ( $K_{eff}$ ). This appears reasonable in that the cant angle of the array being considered is small (on the order of  $10^\circ$ ) so that significant area is not added to the array due



NOTE: SYMMETRY BOUNDARY CONDITIONS  
IMPOSED ALONG BOOM  $\bar{C}$

(a) Planar Solar Array



NOTE:  $K_{eff}$  USED TO  
REPRESENT BOOM  
STIFFNESS WITH IN-  
PLANE BLANKET  
TENSION EFFECT.

(b) "V"-Configuration Solar Array

Figure 24. Symmetric Models

to the change in the projected area. The resulting change in the membrane stiffness due to the small angular rotation should not be significant, but should actually increase the blanket stiffness. Therefore, the main effect seems to be the revised boom stiffness.

Consider the out-of-plane deflections of the "V" stiffened array shown in Figure 25, and the free body diagram of the Leading Edge Member (LEM) shown in Figure 26. These diagrams are identical to those of Reference 7 except for the modified width which now becomes the projected width; i.e.,  $w$  is replaced by  $w \sin \beta$ . The force-deflection relation now becomes:

$$F = \left[ \frac{4 EI}{L^3 (1 + 4 \bar{\alpha})} - \frac{4T}{15 (1 + 4 \bar{\alpha})^2 L} \right] \delta + \frac{Tw \sin \beta}{L} \quad [8]$$

or, neglecting root flexibility

$$F = \left[ \frac{4 EI}{L^3} - \frac{4T}{15L} \right] \delta + \frac{Tw \sin \beta}{L} \quad [8a]$$

and the limiting deflection at which the transition from Region 2 to Region 3 now becomes:

$$\delta_{\text{TRANS}} = Tw \sin \beta \left[ \frac{2 EI}{L^2 (1 + 4 \bar{\alpha})} - \frac{T (1 + 12 \bar{\alpha})}{15 (1 + 4 \bar{\alpha})^2} \right]^{-1} \quad [9]$$

or, neglecting root flexibility,

$$\delta_{\text{TRANS}} = Tw \sin \beta \left[ \frac{2 EI}{L^2} + \frac{T}{15} \right]^{-1} \quad [9a]$$

Using  $K_{\text{eff}}$  to linearize the boom stiffness over the range of applicable deflections and neglecting root flexibility:



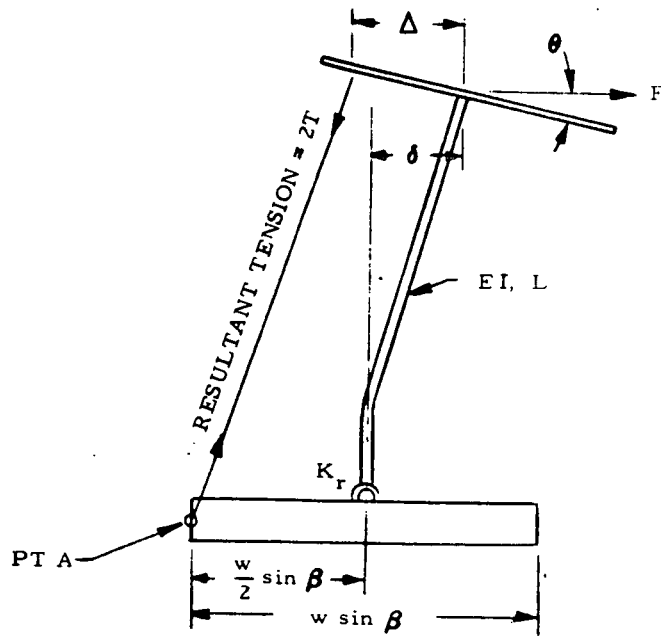


Figure 25. Edge View of Deflected Array

$$V = \frac{6 EI \delta}{L^3 (1 + 4\alpha)} - \left[ \frac{11 + 76\alpha + 160\alpha^2}{5 (1 + 4\alpha)^2} \right] \frac{T \delta}{L}$$

$$M = \frac{2 EI \delta}{L^2 (1 + 4\alpha)} + \frac{T \delta (1 + 12\alpha)}{15 (1 + 4\alpha)^2}$$

Figure 26. Force Diagram to Outer End of Array

$$K_{eff} = \frac{F}{\delta} = \frac{4 EI}{L^3} - \frac{4T}{15L} + \frac{Tw \sin \phi}{L} \frac{1}{\delta} \quad [10]$$

where  $1/2 K_{eff}$  is added to the stiffness matrix of the analytical model at coordinate 17.

It will be noted that the tension effect on the boom stiffness is included in the linearized stiffness. As the tension is increased, the boom stiffness decreases as indicated by the first two terms of Equation [10]. When  $2T = \frac{30 EI}{L^2}$ , the boom stiffness becomes zero and the  $K_{eff}$  is due only to the initial offset value. From the buckling standpoint, the critical buckling load in Region 2 is increased from  $\frac{\pi^2 EI}{L^2}$  to  $\frac{30 EI}{L^2}$ , an increase of approximately 3 to 1.

The mass of the boom is included at the boom tip coordinate using one-fourth of the boom mass.

#### 2.4.4 ASSESSMENT OF STIFFENING EFFECTS

An evaluation of the effectiveness of the "V" stiffened configuration was performed using the basic geometry of the current baseline configuration as a point of reference. This array configuration was postulated to have a cant angle,  $\phi$ , of 10 degrees. The following values were assumed for the parameters specified:

Total deployed length	=	18.565 m (60.9 ft)
Blanket width	=	2.754 m (9.0 ft)
Boom Stiffness (EI)	=	4173 N-m <sup>2</sup> (10,100 lb-ft <sup>2</sup> )
LEM Stiffness (EI)	=	2066 N-m <sup>2</sup> (5,000 lb-ft <sup>2</sup> )
Blanket Weight	=	.135 kg/m (.091 lb/ft)
Tension per Blanket	=	14.2 N (3.2 lb)
Boom Buckling Load	=	114.3 N (25.7 lb)

The analysis was performed for blanket tension values varying from 4.4 to 356 N (1 to 80 lb). For the baseline configuration, the optimum blanket tension was found to be approximately 14.2 N (3.2 lb) so that the tension variation encompasses the values of interest. The resulting force deflection characteristics of the boom are shown in Table 10 in terms of the offset force, and the deflection and force at which the transition to Region 3 occurs. It will be noted that the acceleration requirement of  $7 \times 10^{-4}$  g for the space station mission corresponds to a force of approximately 0.36 N (.08 lbs) so that the small force values listed in the table are actually large for the quiescent environment of space. Comparison of the offset force with the force at transition indicates that the offset provides most of the total transition force for the high tensions and is a major factor in the effective stiffness at transition.

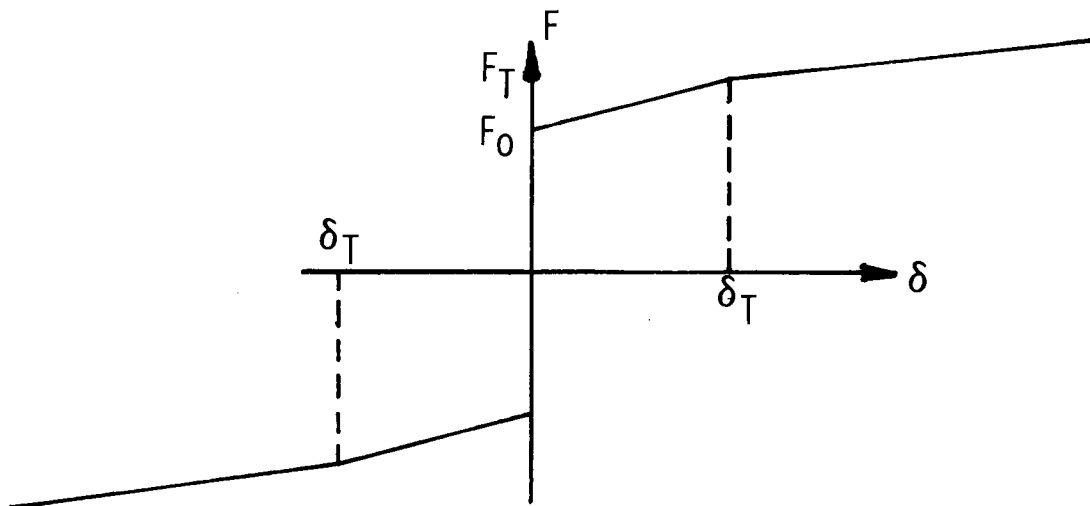
The effect of the cant angle on the array characteristics can be seen from the previous analytical expressions. The deflection at which transition occurs is directly proportional to the sine of the angle (Equation 9a) so that the transitional deflection can be increased, if necessary, by increasing the angle (e.g., a 15 degree angle would result in approximately 50 percent increase in the transition deflection). For a given deflection, the effective boom stiffness is increased significantly due to the increase in the offset force (Equation 10). On the other hand, the effective boom stiffness at the transitional deflection can be shown to be

$$K_{\text{eff}} = \frac{6 EI}{L^3} - \frac{3T}{15 L} \quad [11]$$

which is not affected by the cant angle (i.e., the increase in the transitional deflection compensates for the increase in the force deflection characteristics).

Table 10. Effect of Blanket Tension on Force-Deflection Characteristics of "V" Configuration Solar Array

Blanket Tension per Side (T)		Transition Deflection ( $\delta_T$ )		Symmetric Frequency at $\delta_T$	Offset Force ( $F_0$ )		Transition Force ( $F_T$ )	
(lb)	(N)	(ft)	(m)		(lb)	(N)	(lb)	(N)
40	177.9	7.70	2.347	.1476	1.027	4.568	1.053	4.684
37	164.6	7.31	2.228	.1429	.950	4.226	1.071	4.764
34	151.2	6.89	2.100	.1380	.873	3.883	1.077	4.790
31	137.9	6.45	1.966	.1329	.796	3.541	1.072	4.768
28	124.5	5.98	1.823	.1275	.719	3.198	1.053	4.684
25	111.2	5.49	1.673	.1220	.642	2.856	1.021	4.541
22	97.9	4.97	1.515	.1161	.565	2.513	.974	4.332
20	89.0	4.61	1.405	.1120	.513	2.282	.933	4.150
14	62.3	3.43	1.046	.0985	.359	1.597	.761	3.385
11	48.9	2.78	0.847	.0909	.282	1.254	.644	2.865
10	44.5	2.56	0.780	.0881	.257	1.143	.601	2.673
7	31.1	1.85	0.564	.0789	.180	0.801	.452	2.010
4	17.8	1.09	0.332	.0671	.103	0.458	.275	1.223
2.5	11.1	.70	0.213	.0583	.064	0.285	.181	0.805
1.	4.5	.28	0.085	.0425	.026	0.116	.075	0.334



The fundamental symmetric resonant frequency determined from the analytical model is shown in Figure 27 for the range of tension values investigated. For comparison, the symmetric and antisymmetric frequencies of the baseline planar array are also shown. The "V" array frequency is shown for oscillation amplitudes equal to the transitional deflection and one-tenth the transitional deflection. It should be noted that the small amplitude curve is questionable due to neglecting the Region 1 stiffness. The calculated "V" symmetric frequency trend does not show the flattening effect exhibited by the planar array and indicates that planar array symmetric frequency at the transitional amplitudes can be nearly tripled by increasing the blanket tension of the "V" configuration. It appears that the high blanket tension is indeed realistic since the critical buckling load for the boom for Region 2 is approximately 356 N (80 lb) (e.g., an 89 N [20 lb] blanket tension corresponds to approximately 50 percent of the Region 2 buckling load). Without

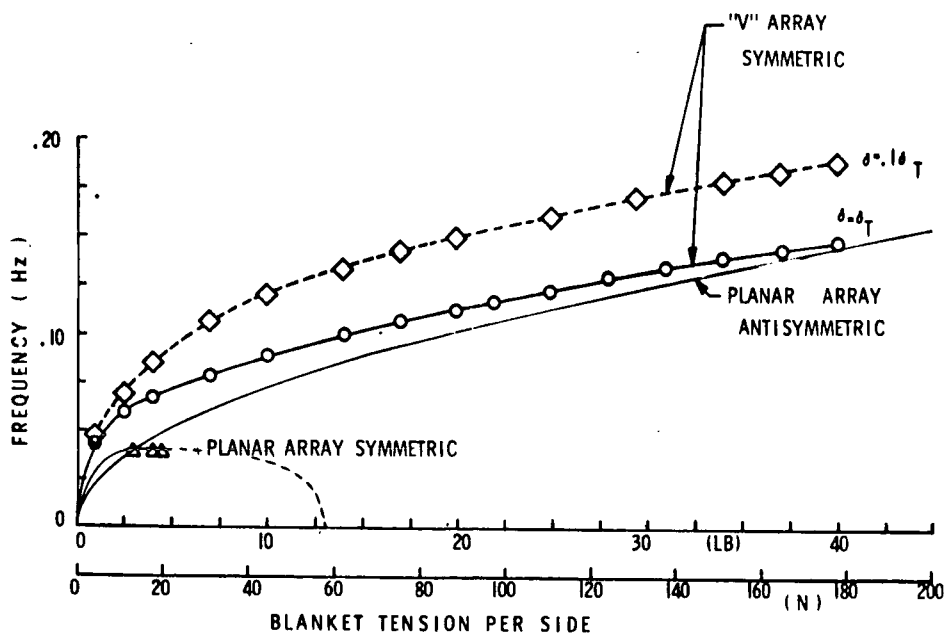


Figure 27. Effect of Blanket Tension on Solar Array Frequency

considering the additional torsional stiffening derived from the "V" configuration, antisymmetric frequencies, approximately three times those of the baseline can be obtained as shown by the planar array antisymmetric frequency variation.

The results of this analysis indicate that the frequencies of the baseline array can be approximately tripled by using the "V" stiffened solar array configuration.

#### 2.4.5 ASSESSMENT OF REDUCED STIFFNESS

In this section, the reduction of the boom stiffness that can be obtained for the baseline configuration is examined. In the previous section, the stiffening effect of the "V" configuration was studied and shown to be highly effective. Another way of taking advantage of the stiffening would be to lower the bending stiffness of the boom while holding the blanket tension constant at a value sufficient to satisfy the .04 Hz frequency requirement. This was studied using a molybdenum boom and neglecting the effect of the "V" shape on the antisymmetric frequency.

For the baseline design, the required blanket tension (per side) of a planar configuration was determined to be approximately 14.2 N (3.2.1b). The tension was set at this value and the boom stiffness varied through the range of practical interest.

The range of boom stiffness that was considered practical was based on the buckling load of the array for the required tension value. If a conservative design approach is used, a criteria that the buckling load of the cantilever boom is not exceeded could be selected. Alternately, a less conservative criteria is that the buckling load of the boom with the blanket restoring moment acting would not be exceeded. Using the first criteria, the boom could not buckle for any range of deflections whereas the second criteria would result in boom buckling if the tip deflection was

greater than the transitional deflection. Using these two criteria, a boom stiffness in the range of 248 to 1240 N-m<sup>2</sup> (600 to 3000 lb-ft<sup>2</sup>) was selected as shown in Figure 28. This approximately spans the buckling load of the boom with and without the blanket tension constraint; i.e., an EI of 1053 N-m<sup>2</sup> (2550 lb-ft<sup>2</sup>) satisfied the first criteria and an EI of approximately 330 N-m<sup>2</sup> (800 lb-ft<sup>2</sup>) satisfies the second criteria. Force-deflection values are summarized in Table 11.

Table 11. Effect of Boom Stiffness on Force-Deflection Characteristic of "V" Configuration Solar Array

Boom Bending Stiffness		Transitional Deflection ( $\delta_T$ )		Symmetric Frequency $\theta \delta_T$	Offset Force		Transition Force	
(lb-ft <sup>2</sup> )	(N-m <sup>2</sup> )	(ft)	(m)		(lb)	(N)	(lb)	(N)
3000	1240	2.73	.832	.0486	.0822	.366	.189	.841
2700	1116	3.00	.914	.0478			.184	.818
* 2400	992	3.32	1.012	.0469			.177	.787
2100	868	3.72	1.134	.0459			.169	.752
1800	744	4.22	1.286	.0449			.158	.703
1500	620	4.89	1.490	.0439			.144	.641
1200	496	5.81	1.771	.0427			.125	.556
900	372	7.16	2.182	.0416	.0822	.366	.096	.427
** 600	248	9.31	2.838	.0404			.051	.227

\* Less than cantilever buckling Load

\*\* Less than constrained buckling load

The calculated symmetric frequencies for this boom stiffness range satisfies the .04 Hz requirement for oscillations at the transitional deflection and a large margin is indicated for smaller oscillation amplitudes. Consequently, the controlling factor is boom buckling.

For the lowest practical value of boom stiffness considered, the transitional deflection of the boom tip is 2.2 m (7.2 ft), and the boom transitional force is

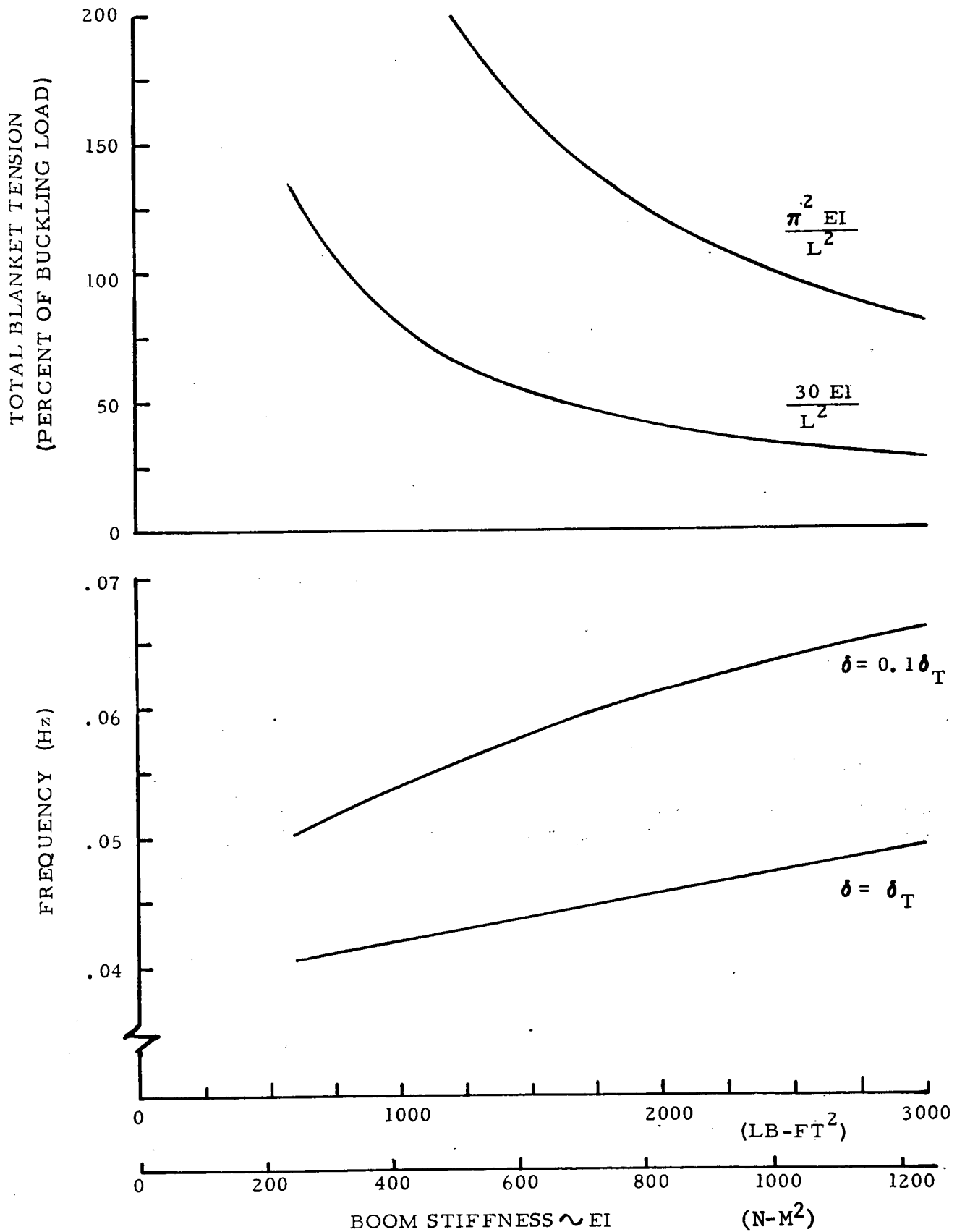


Figure 28. Effect of Boom Stiffness on "V" Configuration Solar Array Characteristics



0.44 N (0.10 lbs). This transitional force appears to compare favorably with the space station mission requirement of  $7 \times 10^{-4}$  g, a 0.36 N (.08 lb) force.

## 2.5 ADVANCES IN THE STATE-OF-THE-ART

### 2.5.1 INTRODUCTION

In Section 2.3, a comparison of deployable boom types has shown that there may be size and weight advantages associated with the use of advanced composite materials for the deployable boom. Several composite materials were investigated for possible application in the deployable boom. A graphite/epoxy composite system has been used by North American Rockwell in the fabrication of a collapsible boom (Reference 8). At the present time, design details and performance data for this boom concept are unavailable for publication. The use of a boron/aluminum composite system for the fabrication of a BI-STEM type deployable boom was investigated with the results reported in Section 2.5.2. This approach appears to be feasible if the monolayer tape material can be obtained with high enough matrix transverse mechanical properties to allow fabrication with a reasonable low boom d/t ratio.

The use of welded solar array interconnections is indicated by the specified temperature extremes and by the requirement to minimize solar cell blanket weight. Section 2.5.3 includes a summary of the existing state-of-the-art in this area. More work is required to apply this technology to the welding of the ultrathin solar cells.

### 2.5.2 BORON/ALUMINUM BI-STEM

#### 2.5.2.1 Introduction

The boron/aluminum matrix composite system has potential as a reduced weight alternate to conventional metals in the fabrication of a BI-STEM type deployable boom

element. In the reinforced direction, this composite system has a strength-to-density and modulus-to-density ratio which is superior to any engineering alloy which is commonly used for BI-STEM elements.

The purpose of this section is to review the status of existing technology in the area of boron/aluminum composite material and to assess the impact of its use in the fabrication of a BI-STEM boom element.

#### 2.5.2.2 Existing B/Al Composite Technology

##### 2.5.2.2.1 Fiber

The composites are fabricated using boron or BORSIC\* fibers. A 102  $\mu\text{m}$  diameter boron fiber has an axial modulus of  $3.86 - 3.93 \times 10^{11} \text{ N/m}^2$  ( $56-57 \times 10^6 \text{ psi}$ ) and has an ultimate tensile strength of about  $3.1 \times 10^9 \text{ N/m}^2$  (450,000 psi). The BROSIC fiber permits fabrication at higher temperatures and has superior oxidation resistance. BORSIC fibers, in diameters of 107 and 142  $\mu\text{m}$ , have ultimate tensile strengths which are approximately 10% lower than uncoated boron fiber as it is currently produced. The fibers are produced by depositing boron onto a 12  $\mu\text{m}$  diameter tungsten substrate. The BORSIC fibers have an additional 3  $\mu\text{m}$  thick coating of SiC on the outside of the boron fiber.

##### 2.5.2.2.2 Matrix Material

Aluminum alloys 2024, 6061, 5052, SAP, 713, 1100 and 1145 have been used as the matrix, including both foil and plasma sprayed prealloyed powder. The properties of the matrix allow have a strong influence on the transverse properties of the composite as discussed in Section 2.5.2.4.

---

\* United Aircraft Corporation trade name for a silicon carbide coated boron fiber.

#### 2.5.2.2.3 Processing

The formation of the composite by placing the fibers in the aluminum matrix alloy can be accomplished by several processes which include: hot pressure bonding, step pressing, roll bonding, plasma spraying and liquid infiltration (Reference 9).

##### (a) Hot Pressure Bonding

In this process, the fibers are precollimated, usually by winding onto a large diameter mandrel, to provide the desired spacing. An organic binder (acrylic, or polystyrene), which is subsequently removed by volatilization during the hot pressing cycle, is used to hold the fibers together. The collimated filament mat is sandwiched between two wrought foil layers which are forced to flow between the filaments by the application of heat and pressure. If the foil surfaces are clean and oxide free, diffusion bonding will occur. The step pressing and roll bonding processes utilize the same principles as the hot pressure bonding process to produce monolayer tape material on a semi-continuous and fully continuous basis, respectively. With the step pressing process, diffusion bonded monolayer tape is produced by a continuous series of overlapping flat die bonding cycles. Typical consolidation parameters for a boron/aluminum composite with 50 v/o filaments are 1 hour at  $48.3 \times 10^6$  N/m<sup>2</sup> (7,000 psi) and 480°C (900°F).

##### (b) Plasma Spraying

In this process, the filaments are wound onto a large diameter mandrel over a foil layer. The mandrel is rotated and traversed before the plasma arc. The diameter of this mandrel restricts the

length of tape that can be produced by the plasma spraying process. At United Aircraft, the existing equipment restricts this length to approximately 3.65 m (12 ft). Aluminum alloy powder, which is injected into the hot gas of the plasma arc, is melted into droplets which deposit on the foil and fiber to form the monolayer tape composite. The sprayed matrix is not fully dense and therefore must be consolidated by hot pressure bonding or braze bonding. The strength of boron fibers has been observed to degrade as a result of contact with the molten aluminum droplets. The use of BORSIC fibers overcomes this problem and BORSIC/aluminum composites with a variety of matrix alloy compositions have been produced.

(c) Liquid Infiltration

With this process, continuous filaments are passed through the molten matrix alloy into an orifice of the desired geometry to produce a continuous composite rod. Chemically inert coatings of the boron fibers are required to prevent reaction with the molten aluminum alloys. General Technologies Corporation (GTC) used BORSIC fiber to provide continuous tape material. A boron nitride coated boron fiber has been used with the liquid infiltration process to produce a monolayer tape which is marketed under the trade name NITBORAL by Monjoe Scientific. Suitable matrix materials are limited to certain casting alloys which have the ability to wet the filaments. For this reason, it is not possible to achieve matrix strengths which are equivalent to hot pressed composites.

#### 2.5.2.2.4 Sources of Supply

Boron/aluminum monolayer tape material is available from any of the following sources:

1. Hamilton Standard Division of  
United Aircraft Corporation  
Windsor Locks, Connecticut 06096
2. Amercom, Inc.  
9060 Winnetka Avenue  
Northridge, California 91324
3. Union Carbide Corporation  
P. O. Box 24184  
Indianapolis, Indiana 46224
4. AVCO-Systems Division  
Lowell Industrial Park  
Lowell, Massachusetts 01851
5. Martin-Marietta Aluminum  
19200 S. Western Avenue  
Torrance, California 90509

#### 2.5.2.3 Environmental Stability

##### 2.5.2.3.1 Salt Exposure

Exposure of 2024 and 6061 matrix BORSIC/Aluminum composites to a salt spray at 35°C resulted in corrosion of the matrix material that was most severe with the 2024 alloy in the as-fabricated condition. All specimens were loaded in flexure in a three-point bend fixture. Matrices of 6061-F and 6061-T6 exhibited general corrosion without preference for regions of high stress whereas the 2024 matrices displayed greater depths of attack on the tensile surfaces as compared to the compression surfaces.

##### 2.5.2.3.2 Thermal Cycling

Thermal cycling of 50 percent by volume 107  $\mu\text{m}$  BORSIC/6061-F aluminum composites between 21°C and 354°C can cause void formation within the matrix as a result of

plastic strains caused by differences in thermal expansion among the constituents. These voids result in decreased density and reduced flexural strength which amounts to about 13% for unidirectional material after 5000 cycles.

#### 2.5.2.4 Composite Material Properties

The modulus of elasticity in the longitudinal direction is strongly influenced by the fiber content as shown in Figure 29. Table 12 gives the ultimate tensile strength in the axial direction for several BORSIC/Aluminum composites.

Table 12. Axial Tensile Strength of 142  $\mu$ m BORSIC/Al  
(From Reference 11)

Matrix	v/o Boron (%)	Ultimate Tensile Strength ( $10^3$ psi)	Elastic Modulus ( $10^6$ psi)	Strain to Fracture (%)
2024F	45	185.7	30.4	0.765
	45	197.5	27.5	0.835
	44	177.0	30.0	0.725
	47	212.0	32.0	0.825
	47	212.0	32.6	0.820
	49	194.0	32.0	0.740
2024-T6	46	202.5	32.8	0.75
	46	213.6	31.6	0.81
	47	217.0	32.3	0.830
	48	213.0	31.3	0.845
	64	279.0	40.0	0.755
2024F	70	279.5	----	-----
	66	253.0	----	-----
	67	250.2	----	-----
6061F	48	196.3	31.8	0.710
	48	171.0	28.2	0.590
	50	204.0	33.8	0.72
	50	208.0	32.0	0.76
6061-T6	52	216.5	33.8	0.78
	51	197.0	33.4	0.69
	50	203.0	----	-----

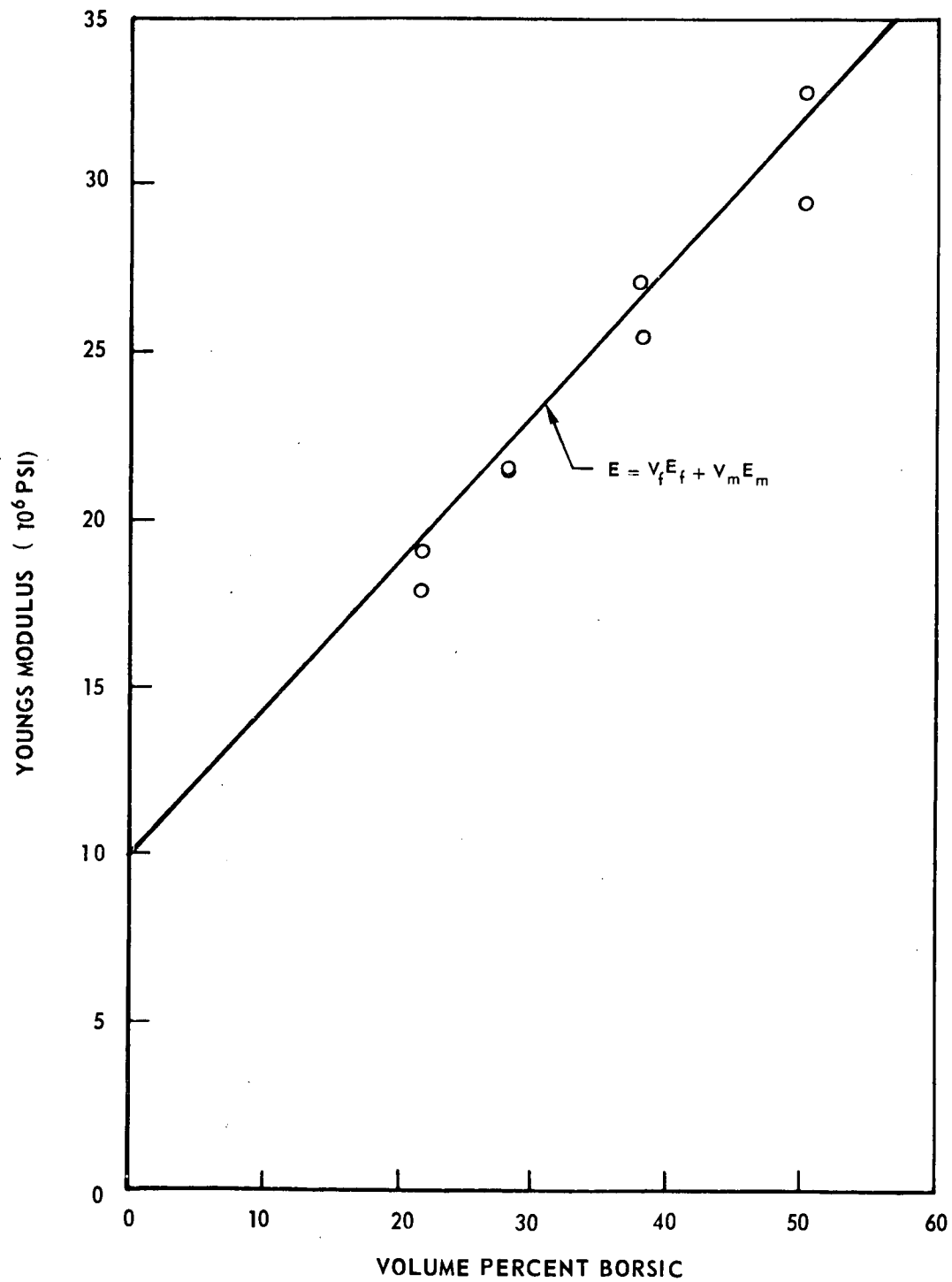


Figure 29. Effect of Fiber Content on Composite Modulus of Elasticity (from Reference 10)

In the transverse direction, the mechanical properties of the composite are greatly influenced by the matrix material. For the composites studied by United Aircraft, the components were BORSIC fiber and a matrix consisting of foil and plasma sprayed material. The plasma sprayed portion of the matrix can contain as much as 10 to 15% porosity in the as-sprayed condition. If some of this porosity is permitted to remain, the strength of the matrix will be severely reduced. The use of hot press diffusion bonding of the matrix has reduced the effect of this porosity. The transverse elastic modulus is a sensitive indicator of the degree of composite consolidation and bonding and thus can be used as a criteria for determining the integrity of the composite.

Figure 30 shows the transverse elastic modulus as a function of volume fraction of 107  $\mu\text{m}$  diameter BORSIC. This figure shows that the transverse elastic modulus in-

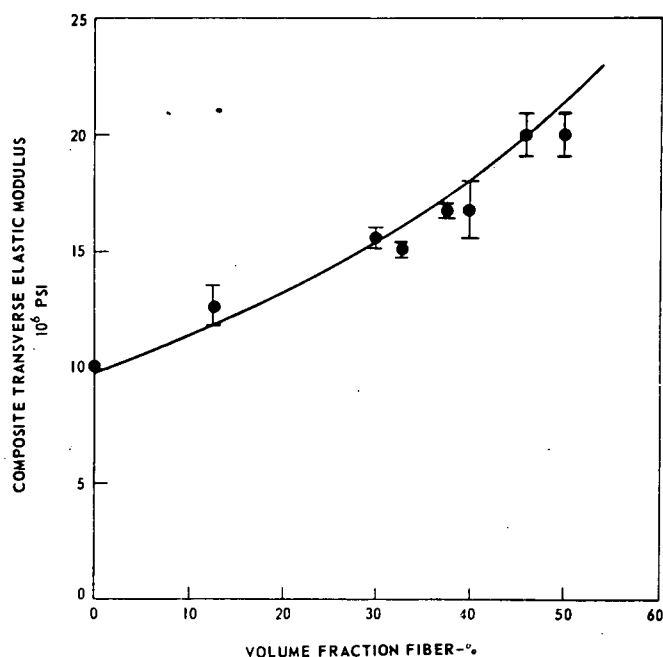


Figure 30. Transverse Elastic Modulus vs. Content of 107  $\mu\text{m}$  BORSIC Fibers (from Reference 11)



creases with increasing volume fraction of fibers.

The transverse tensile strength of 107  $\mu\text{m}$  diameter BORSIC fiber composites as a function of matrix material tensile strength is shown in Figure 31. Three distinct regions of behavior are evident on this figure. In Region I, the composite strength is approximately equal to the matrix strength. In this region, the matrix fails at an applied stress below that required for fiber failure. Thus, fracture surfaces of failed composites exhibit only a small amount of split fibers. In Region II, the composite strength is relatively independent of matrix strength. Fracture surfaces exhibit a large amount of fiber splitting since the matrix strength is sufficient to cause loading of the fibers to their ultimate transverse strength prior to composite failure. This fiber failure causes an overload in the matrix material which results in composite fracture since the matrix material does not have the

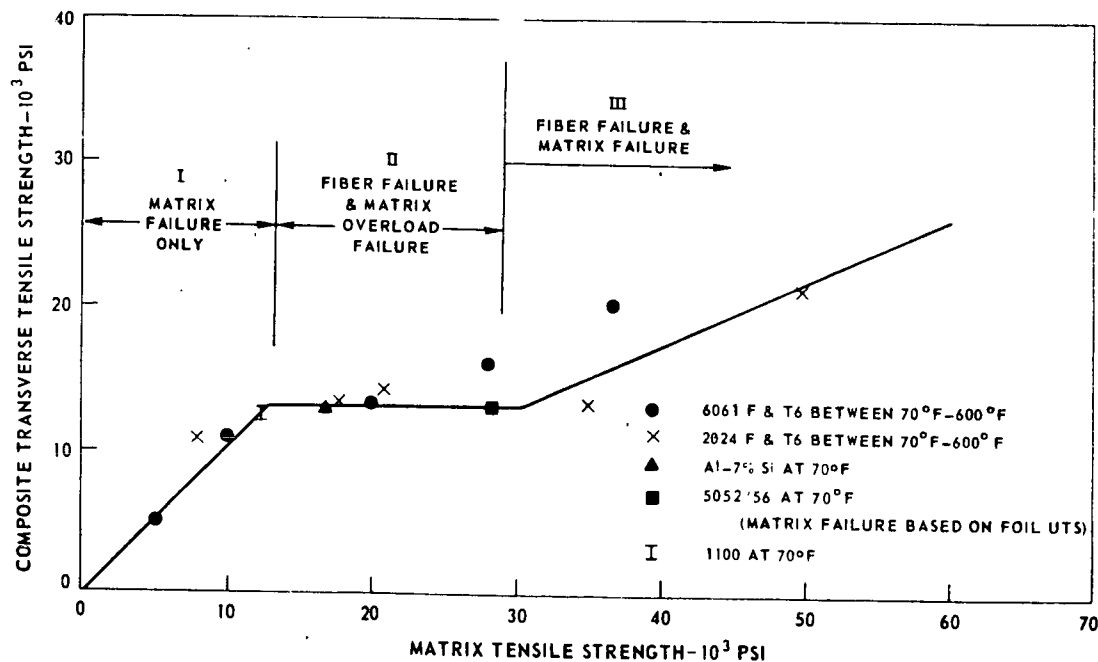


Figure 31. Transverse Tensile Strength of 50% Volume 107  $\mu\text{m}$  BORSIC/Aluminum (from Reference 11)

necessary strength to prevent total composite failure subsequent to fiber splitting. In Region III, as in Region II, the matrix strength is sufficient to cause fiber splitting prior to composite failure. However, in Region III, the matrix strength is sufficient to prevent immediate overload failure. Thus, the composite strength is determined by the net section of load bearing matrix remaining, subsequent to fiber failure, and the strength of this matrix.

The large diameter ( $\approx 142 \mu\text{m}$ ) BORSIC fibers, which have a larger ratio of boron to tungsten core, exhibit much higher transverse fiber strengths than the smaller diameter fibers. As a result, composites fabricated with these larger diameter BORSIC fibers exhibit very little fiber splitting. The primary mode of failure is matrix rupture. Figure 32 shows that the composite strength is very nearly equal to the matrix strength.

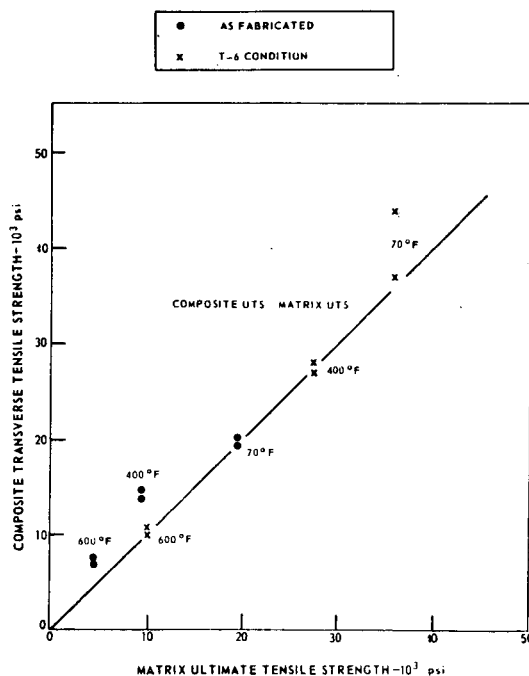


Figure 32. Transverse Tensile Strength of 60% by Volume  $142 \mu\text{m}$  BORSIC/6061 Aluminum (From Reference 11)

#### 2.5.2.5 Application to a BI-STEM Type Deployable Boom

The performance of a BI-STEM deployable boom element which is fabricated from B/Al composite material was analyzed. The composite tape material was postulated to be of a configuration as shown in Figure 33. Figure 34 shows some possible configurations of the monolayer tape as a function of volume percent boron fiber. Two nominal fiber diameters have been shown to illustrate the dependence of tape thickness on fiber spacing and content. For example, with a 142  $\mu\text{m}$  fiber diameter and with a 50% fiber content by volume, a tape thickness of 178  $\mu\text{m}$  can be achieved with a 178  $\mu\text{m}$  fiber spacing. This thickness is commonly available, with a wrought foil layer top and bottom, from the sources listed in Section 2.5.2.2.4. In the formation of a BI-STEM type element from this monolayer tape material, the fiber direction is along the deployment direction of the boom element. Thus, the longitudinal

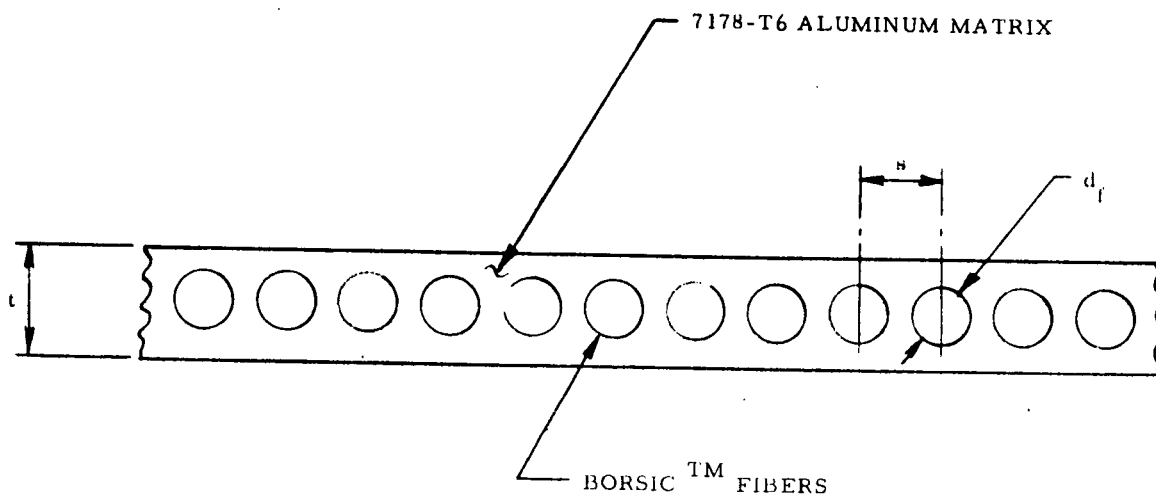


Figure 33. B/Al Composite Tape Material

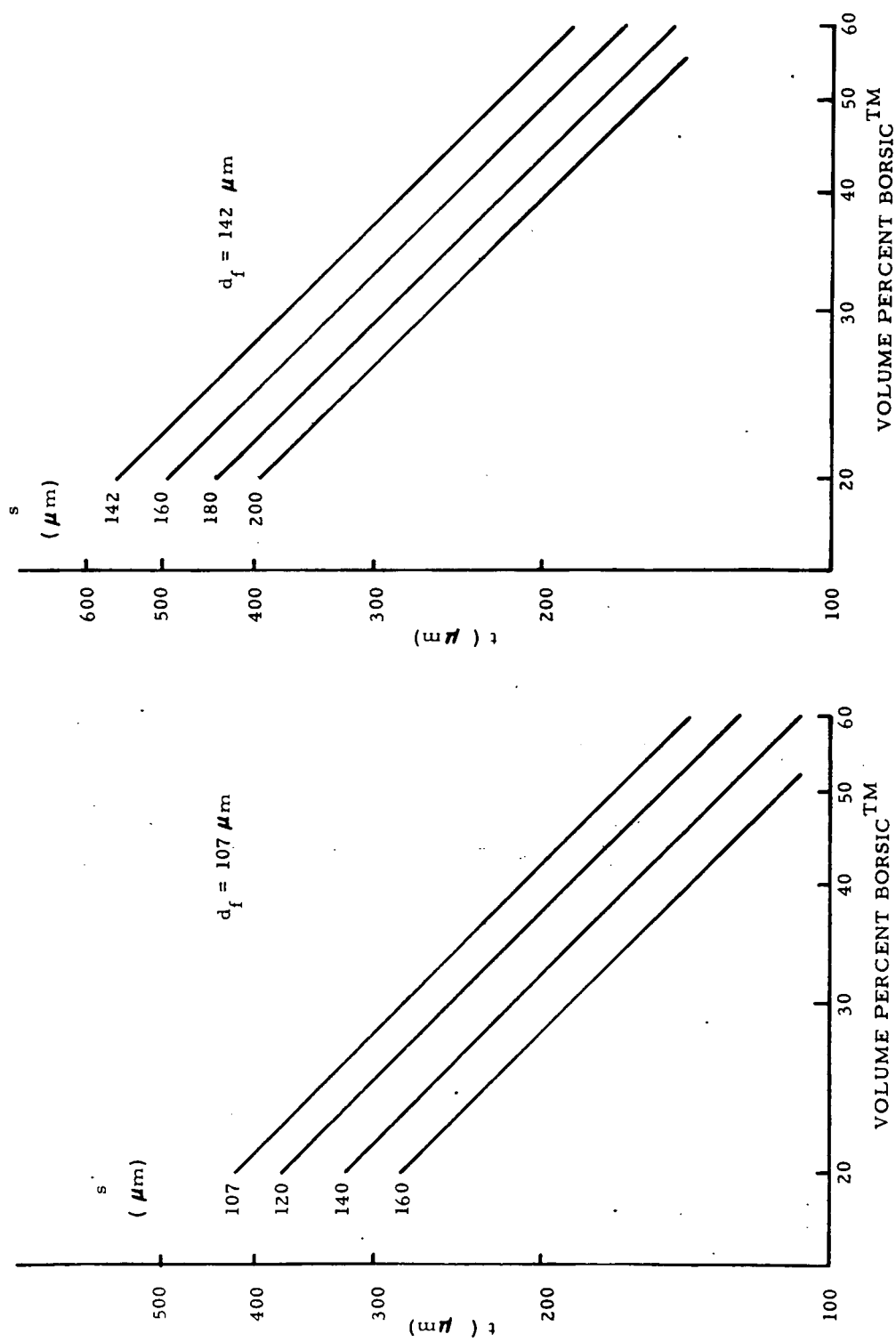


Figure 34. Possible Configurations of B/AI Monolayer Tape

modulus of elasticity of the composite is influenced by the BORSIC fiber content as shown in Figure 29. For a BORSIC fiber content of 50 percent by volume, the modulus of elasticity in the longitudinal direction will be about  $20.7 \times 10^{10} \text{ N/M}^2$  ( $30 \times 10^6 \text{ psi}$ ). In the transverse direction, which is the forming direction of the BI-STEM C section, it is necessary to have a matrix with a high enough tensile strength to elastically accommodate the strain associated with the flattening of the C shape. Assuming a minimum d/t ratio of 300 (see Figure 35), the aluminum alloy at the outer most fiber of the strip must be capable of elastically accommodating a strain of .0033. If a 7178 matrix alloy were used, it might be possible to achieve this low a d/t ratio. Table 13 lists the mechanical properties of the higher strength aluminum alloys.

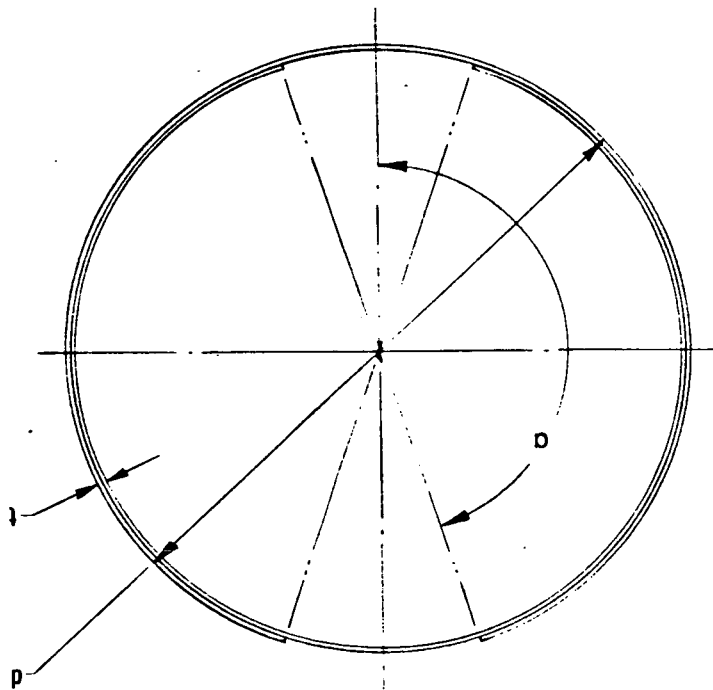


Figure 35. BI-STEM Section

Table 13. Properties of Aluminum Alloy Matrix Materials\*

ALLOY AND TEMPER	ULTIMATE TENSILE STRENGTH		TENSILE YIELD STRESS		MODULUS OF ELASTICITY		DENSITY	
	(PSI)	(N/m <sup>2</sup> )	(PSI)	(N/m <sup>2</sup> )	(PSI)	(N/m <sup>2</sup> )	(lb/in <sup>3</sup> )	(gm/cm <sup>3</sup> )
2024-T4	64,000	4.41x10 <sup>8</sup>	40,000	2.76x10 <sup>8</sup>	10.5x10 <sup>6</sup>	7.24x10 <sup>10</sup>	0.100	2.77
6061-T6	43,000	2.96x10 <sup>8</sup>	38,000	2.62x10 <sup>8</sup>	9.9x10 <sup>6</sup>	6.83x10 <sup>10</sup>	0.098	2.72
7075-T6	78,000	5.37x10 <sup>8</sup>	69,000	4.75x10 <sup>8</sup>	10.3x10 <sup>6</sup>	7.10x10 <sup>10</sup>	0.101	2.80
7178-T6	85,000	5.85x10 <sup>8</sup>	75,000	5.16x10 <sup>8</sup>	10.3x10 <sup>6</sup>	7.10x10 <sup>10</sup>	0.102	2.83

\* Values from Reference 12.

For the BI-STEM section shown in Figure 35, the minimum moment-of-inertia is given by:

$$I_{11} = \frac{d^3 t}{4} \left[ 1 + \sin \alpha \cos \alpha - \frac{2 \sin^2 \alpha}{\alpha} \right] \quad [12]$$

Also the strip width, w, is given by:

$$w = \lambda d$$

where  $\lambda$  = overlap factor

For the case where  $\lambda = 0.90$  ( $\alpha = 162$  deg.), equation [12] reduces to:

$$I_{11} = \frac{d^3 t}{4} (2.46596)$$

Thus, for a tape thickness of 178  $\mu\text{m}$ , the boom diameter is 53.4 mm, and the minimum moment-of-inertia is 16710 mm<sup>4</sup>. With the 50% B/A1 composite, the boom bending stiffness is 3456 N-m<sup>2</sup>, and the element weight is 0.142 kg/m of length.

### 2.5.3 WELDED SOLAR CELL INTERCONNECTORS

#### 2.5.3.1 Introduction

The use of a welded connection between the solar cell contacts and the interconnector is a potentially attractive choice for use on the 110 watt/kg solar array system. The purpose of this section is to describe the differences and relative merits of welded vs. soldered interconnectors and to summarize the present state-of-the-art in welded solar cell interconnectors. The choice of interconnector joining method for this feasibility study is strongly influenced by the thermal shock environment. As specified in Reference 1, this shock is between the extremes of  $-190$  and  $+140^{\circ}\text{C}$  for a total of 1000 complete cooling and heating cycles.

#### 2.5.3.2 Comparison of Welded Soldered Interconnections

Table 14 summarizes the relative advantages and disadvantages of soldered and welded solar cell interconnections. Within the U.S. soldered solar cell interconnections have been exclusively used on flight solar arrays with satisfactory performance under most conditions of temperature and cycle life imposed by earth orbiting missions. The requirement for low temperature ( $<-120^{\circ}\text{C}$ ) and/or high temperature ( $>120^{\circ}\text{C}$ ) operation raises questions concerning the applicability of the soldered interconnection. Thermal cycling to a low temperature extreme causes high stresses in the solder which results in cracks which may propagate into the silicon. The number of such solder cracks increases with decreasing low temperature extreme as shown in Figure 36. The stresses in the solder are greater for interconnector materials which have higher coefficients of thermal expansion than silicon and are also greater for thicker interconnectors of the same material.

At the high temperature extreme, the solder points have low contact strength and are subject to creep under sustained stress. Figure 37 shows the pull test tab

Table 14. Comparison of Soldered and Welded Solar Cell Interconnections

METHOD	ADVANTAGES	DISADVANTAGES
Soldering	<ul style="list-style-type: none"> <li>Acceptable joints with a wide range of process parameters</li> <li>Repair easily performed to replace damaged cells</li> <li>Joint inspection criteria can be based on solder fillets</li> </ul>	<ul style="list-style-type: none"> <li>Solder joints have low peel and creep strength at high temperatures</li> <li>Solder joints may melt under "hot-spot" failure mode conditions such as partial shadowing or open circuit failures</li> <li>Solder may cause silicon flake-out at low temperatures.</li> <li>Solder joint exhibits highest stresses and is the weakest link under thermal cycling</li> </ul>
Welding	<ul style="list-style-type: none"> <li>Lower weight due to the elimination of solder</li> <li>Modules can operate at higher temperatures without failures due to low peel or creep strength</li> <li>Interconnector material can be selected for a close match of the coefficient of thermal expansion to that of silicon, resulting in reduced stresses at low temperatures.</li> </ul>	<ul style="list-style-type: none"> <li>Joint repair is difficult</li> <li>Visually inspection can not insure a good weld</li> <li>Process parameters must be controlled within a narrow range</li> </ul>

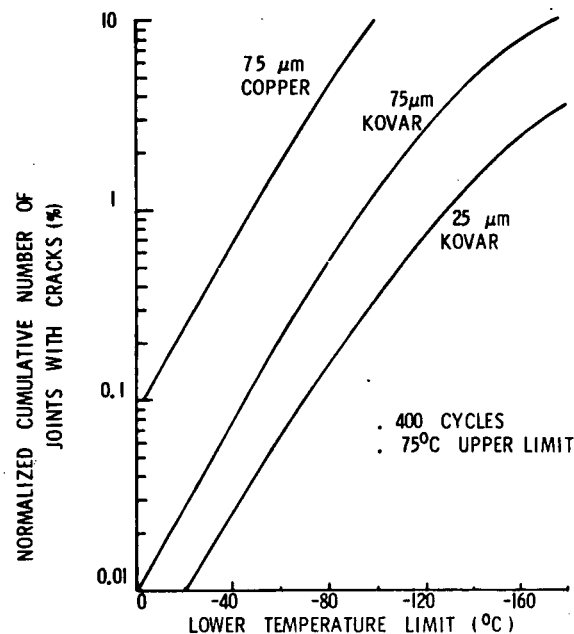


Figure 36. Normalized Cumulative Number of Solder Joints Showing Cracks after 400 Cycles from 75°C to the Indicated Lower Temperature Limit (From Reference 13)



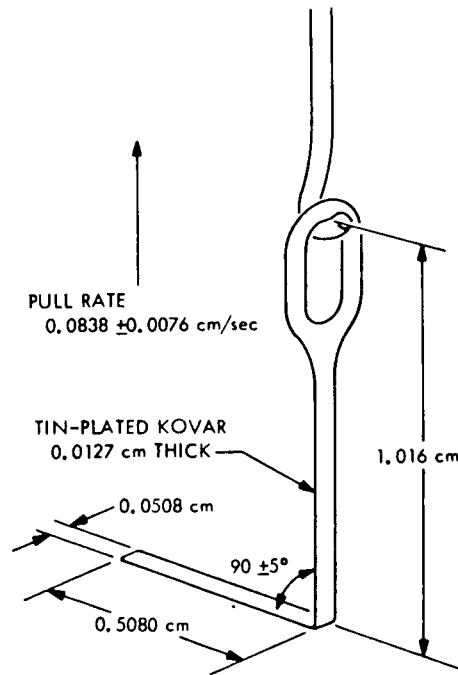


Figure 37. Contact Pull Strength Tab Configuration (From Reference 14)

configuration used to obtain the contact strength results shown in Figure 38. Figure 39 shows the time required for solder joint rupture versus the applied stress for two solder alloys at various temperatures.

The weight savings associated with the elimination of solder will typically amount to about 15 mg/cell or about 3.4 kg for an array of the size required for this study.

### 2.5.3.3 Welded Interconnector State-of-the-Art

#### 2.5.3.3.1 General

Experience with welded solar cell interconnectors is not as extensive as with soldered joints and a large portion of the experience is European based. Four welding methods have been successfully used to join interconnectors to cell contacts.

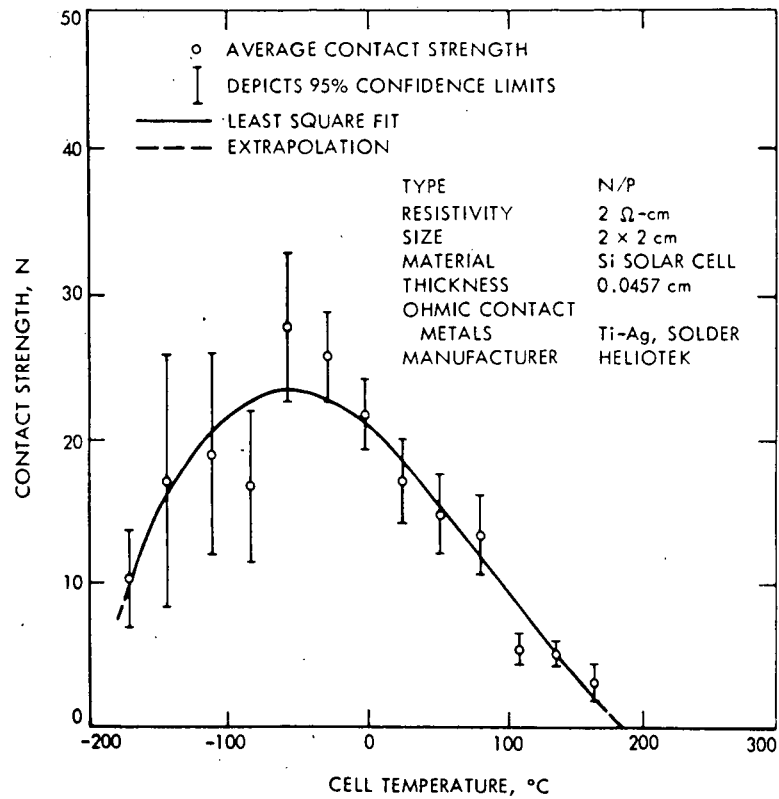


Figure 38. Contact Strength of Solar Cell Solder Joint (From Reference 14)

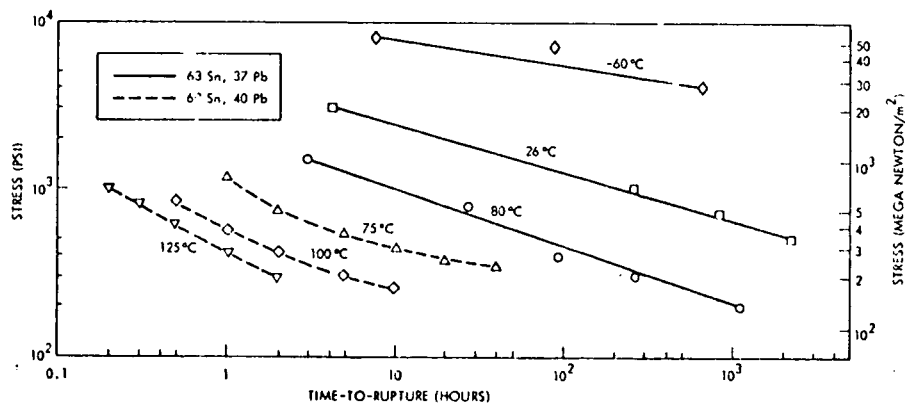


Figure 39. Time To Solder Joint Rupture Versus Applied Stress for Two Solder Alloys at Various Temperatures (From Reference 13)

These are: (1) ultrasonic welding, (2) resistance welding (parallel gap), (3) laser welding and (4) thermal diffusion/thermal compression welding.

#### 2.5.3.3.2 Ultrasonic Welding

Ultrasonic welding is a highly attractive approach for solar cell interconnector joining because it does not produce high temperature beyond a very shallow depth from the weld interface. The ultrasonic welding of aluminum interconnectors to aluminum contacted solar cells has been performed by TRW (Reference 15) and by Hughes (Reference 16).

The TRW interconnectors were cut from notched 1100-0 aluminum strip material which is 75  $\mu\text{m}$  thick by 3 mm wide. Welding was performed using the following welding equipment: (1) weld head, Unitek Model 1-144-01; (2) Unitek Power Supply Model 2-130-D1; and (3) Transducer Sonobond Model W-260-A. Figure 40 shows the two

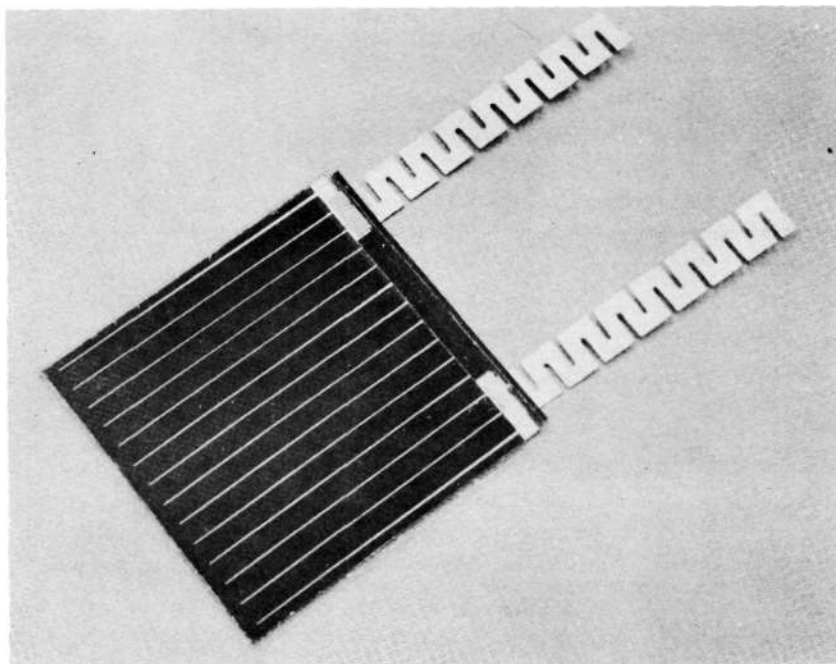


Figure 40. TRW Welded Aluminum Interconnector Configuration (From Reference 15)

interconnector strips welded to the top contacts. As shown in the figure, cover-glass covers the entire top surface of the cell including the bar contact and weld joints. In addition, there is a Kapton strip which is bonded between the cover-glass and the cell to function as a shield over the aluminum interconnector in the gap between cells.

The aluminum interconnector has a much higher coefficient of thermal expansion than the silicon with the result that high stresses are created in both the silicon and the aluminum at the weld joints during thermal cycling. Figure 41 shows the calculated stresses in the aluminum at a temperature of  $-180^{\circ}\text{C}$  normal to the cell surface acting to pull the welded joint apart. Figure 42 shows the calculated number of cycles to failure for the weld joint as a function of temperature extremes.

Four panel segments of this welded construction (each panel segment consisting of two  $20\text{s} \times 2\text{p}$  modules) were subjected to five temperature cycles between  $-100^{\circ}$  and  $+100^{\circ}\text{C}$  without evidence of performance degradation.

The Hughes aluminum interconnect/aluminum contact ultrasonic welding process was developed for use on the Air Force Hardened Solar Power System (HASPS). Figure 43 shows a module which was interconnected using this welding process. In addition to the aluminum-to-aluminum weld, Hughes has ultrasonically welded aluminum interconnectors to solderless Ti-Ag contacted solar cells (References 16 and 17). Each weld was accomplished in a few seconds at room temperature using a Sonoweld Model W-1040 TSL weld system with a specially designed tip. Pull strength data has shown these welds to be satisfactory and comparable to the all aluminum system. Because of the concern about the aluminum-silver galvanic couple, those welded cells were subjected to extreme humidity testing which consisted of 168 hours at  $85^{\circ}\text{C}$  and approximately 95 percent relative humidity. Post test examination revealed no

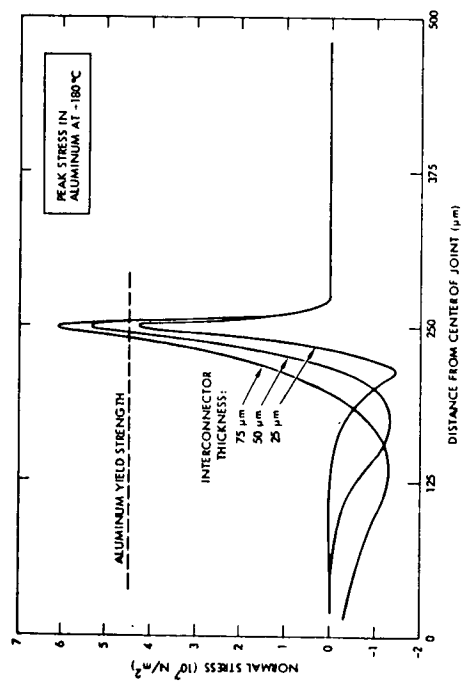


Figure 41. Thermal Stress in Welded Joints  
(From Reference 15)

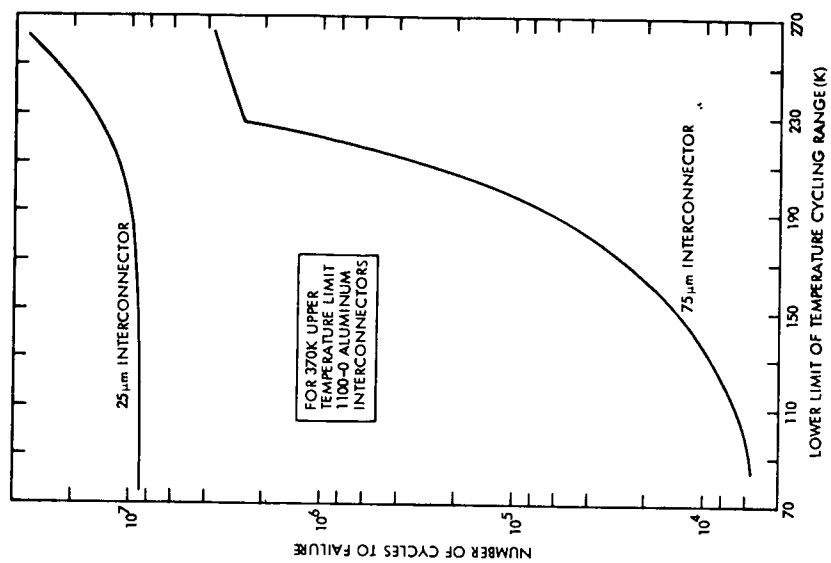


Figure 42. Cycles to Failure versus  
Temperature Cycling Range (From  
Reference 15)

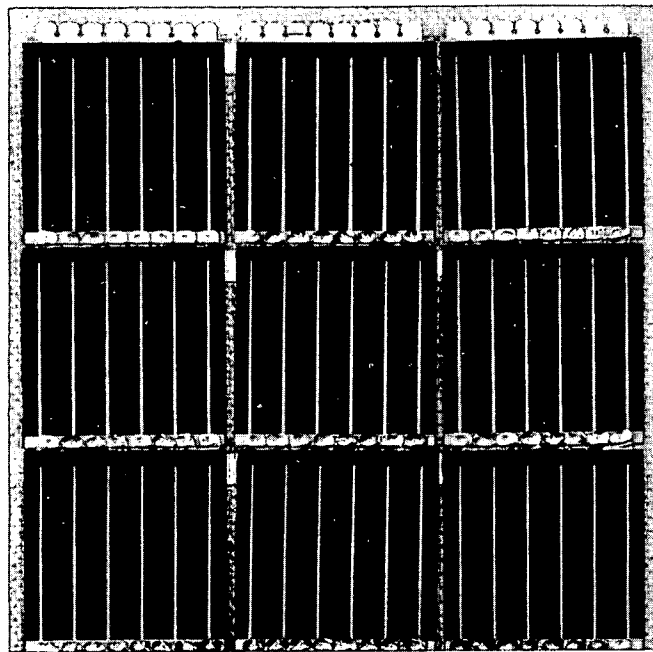


Figure 43. Hughes Aluminum Cell/Aluminum Interconnector  
Ultrasonically Welded Module (From Reference 16)

visible discoloration or corrosion of the weld area or interconnect and electrical testing showed no measurable effect.

#### 2.5.3.3.3 Resistance Welding (Parallel Gap)

Resistance welding uses the heat generated by an electric current passing through the workpiece in the space between two closely spaced electrodes which are pressed against the piece. The resulting melting in the current path can produce a weld between the interconnect material and the solar cell contact metallization.

Resistance welding of solar cell interconnectors has been performed by Messerschmitt-Bölkow-Blohm (MBB)/Siemens AG., AEG-Telefunken, and BAC/Turner. A summary of this technology which is supported by ESRO is contained in Reference 18. Resistance welding was selected over the other two methods because it gave more



reproducible bonds than ultrasonic welding and did not require heating the whole solar cell to a high temperature as in thermal diffusion bonding. A potential problem with resistance welding is a degradation of the shallow junction during welding since a typical weld pulse releases 10 joules in 10 msec over an area of  $0.3 \text{ mm}^2$ . In the ESRO sponsored work, it was possible to determine a range of welding parameters when high bond strength could be obtained without junction damage.

Figure 44 shows a resistance welded connection between Ag expanded metal and a Ti(Pd)Ag solar cell front contact. Figure 45 shows a photomicrograph of the joint. These welds were obtained using a Hughes impulse welder model MCW-550 with a parallel gap bonding head VTA-66MV. Symmetrical molybdenum carbide electrodes with rectangular tips were used. This machine, shown in Figure 46, provides electronic control of the weld voltage and pulse duration.

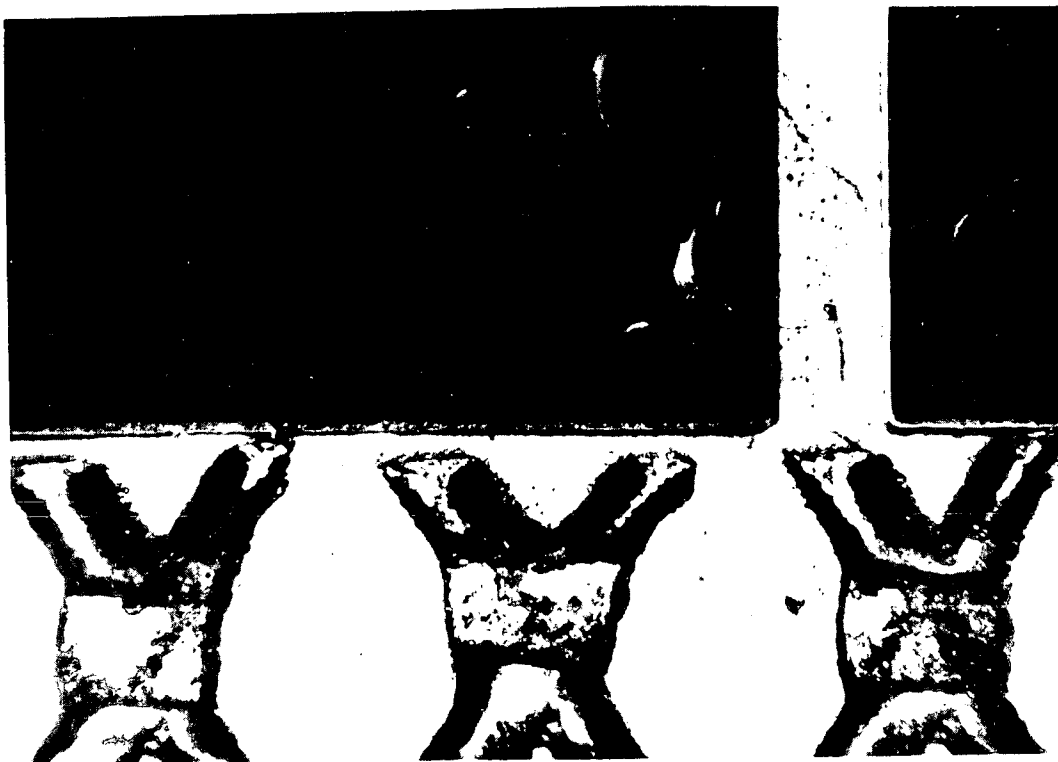


Figure 44. Welded Ag Mesh Interconnector (From Reference 19)

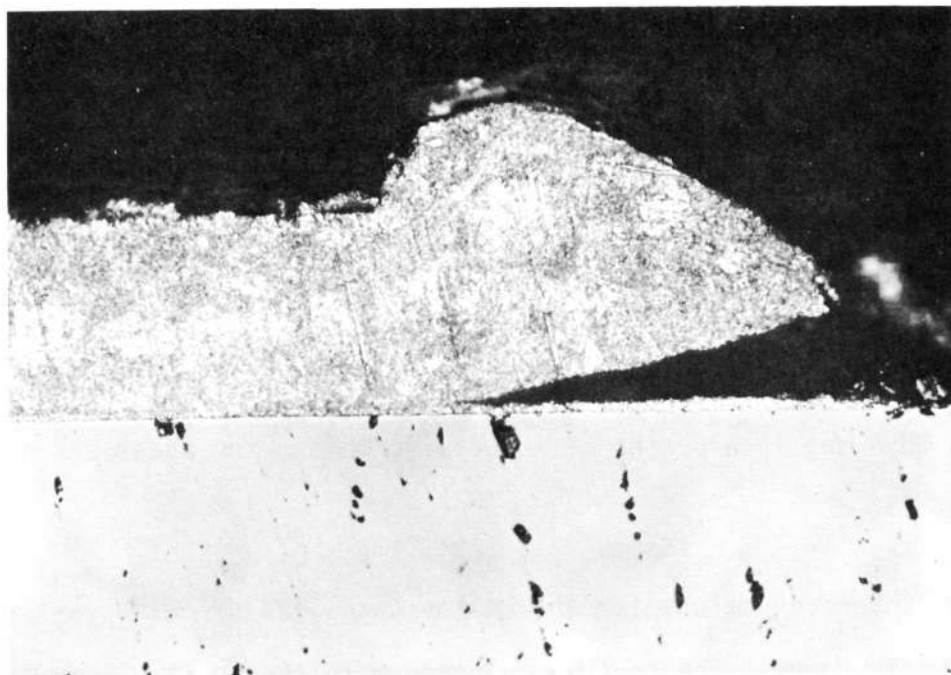


Figure 45. Photomicrograph of Welded Joint (From Reference 19)

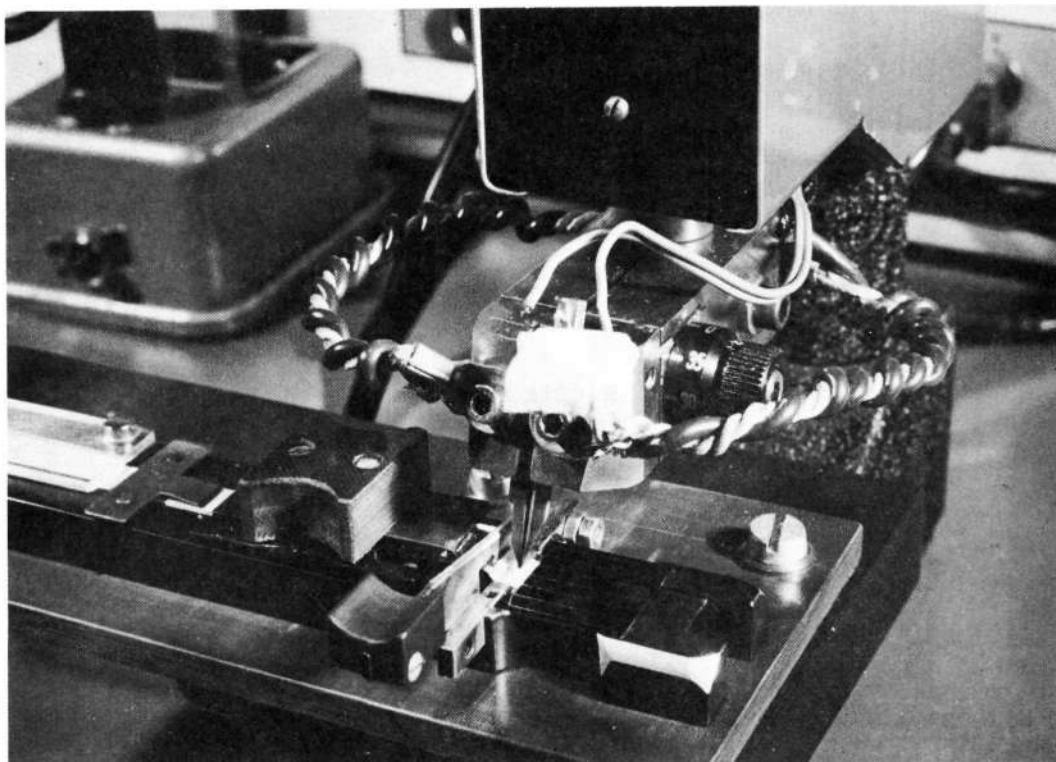


Figure 46. Hughes MCW-550 Impulse Welder (From Reference 19)



AEG Telefunken has resistance welded silver plated molybdenum interconnectors to Ti(Pd)Ag cell contacts. The molybdenum thickness was 30  $\mu\text{m}$  and the optimum silver coating thickness was found to be 5  $\mu\text{m}$ . A pulse duration of 100 msec at a voltage of 0.65 v was found to give strong, reliable bonds with no obvious damage to the silicon. At the end of the optimization study, the shear strength of the welded tabs exceeded 30 N and in a series of successive welds, the shear strength did not vary more than 25%.

The solar cell interconnections for the Helios satellite are also resistance welded silver plated molybdenum. The nominal molybdenum thickness is 20  $\mu\text{m}$  with 5  $\mu\text{m}$  of silver plating on each side using a thin platinum interlayer for improved adherence (Reference 20). The selection of weld parameters was based on the mechanical strength of the weld and the electrical degradation of the cell. Figure 47 shows these two measures of performance as a function of welding voltage. Pull strength increases with increasing voltage. The

electrical degradation, which results from diffusion of contact material through the p-n junction, occurs at higher voltages. The final welding voltage range was selected so that the pull strength is sufficiently high with negligible electrical degradation. The silver metallization on the cell contact

was chosen to be  $10 \pm 3 \mu\text{m}$  thick and the optimum weld pulse duration was found to be 200 msec. As a qualification test, the

solar cell modules were subjected to a temperature cycling test which consisted of 4 days at  $-85^\circ\text{C}$  followed by 10 days at  $+200^\circ\text{C}$ . This cycle was repeated for a total

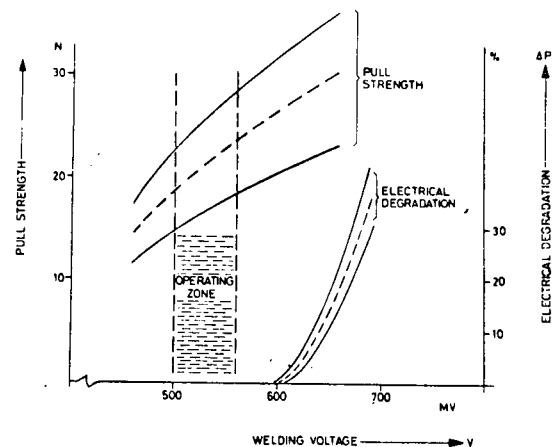


Figure 47. Mechanical Strength of Weld and Electrical Degradation versus Welding Voltages (From Reference 20)

test duration of 6 weeks.

A limited number of welds have been made on solar cells with plated Ni/Cu/Ni/Au contacts. Interconnectors of pure gold and gold plated molybdenum were used. The welds had a good shear strength and did not fail in thermal cycling and humidity storage (Reference 18).

#### 2.5.3.3.4 Laser Welding

The use of a pulsed ruby laser welder to join silver and silver plated molybdenum interconnectors to Ti-Ag solar cells has been implemented by Hughes as reported in Reference 16. The laser welder, shown in Figure 48, uses an optically focused beam of pulsed coherent radiation, such as red light ( $0.6943\text{ }\mu\text{m}$ ). This method of welding offers flexibility in spot size and shape control as well as control over the amount of heating at the cell junction. The molybdenum interconnector material was

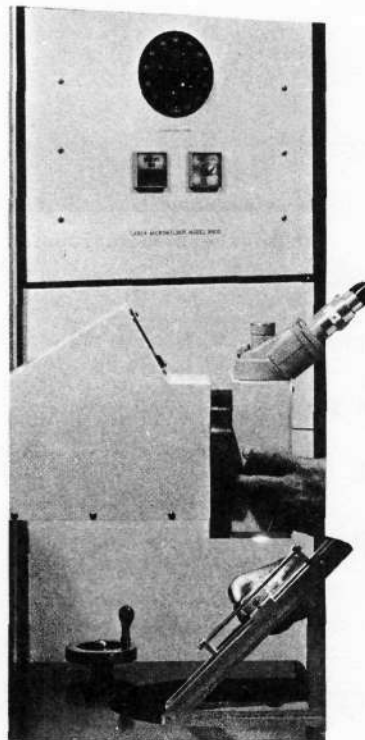


Figure 48. Laser Microwelder (From Reference 16)

found to be well suited to laser welding with the best results achieved when the molybdenum was plated on only one side thereby letting the laser impinge on the exposed molybdenum. Microsections of laser welds revealed adequate welding, but voids were often present, possibly due to the fact that the pulse duration was too short to permit venting of absorbed or trapped gas at the weld interface.

#### 2.5.3.3.5 Thermal Diffusion/Thermal Compression Welding

The Boeing Company has utilized this method to join expanded silver mesh interconnectors to solderless Ti-Ag contacted solar cells (Reference 21). The process has yielded acceptable joints with peel strengths as shown in Figure 49. Test samples have been subjected to 10 rapid temperature changes from +100 to -190°C with no apparent degradation in electrical or mechanical integrity.

The application of this process on a production basis is limited by the following drawbacks: (1) bonding must be accomplished in a vacuum, (2) the long time required to form the joints, and (3) the number of cells that can be interconnected at the same time is limited by the tooling and vacuum facility.

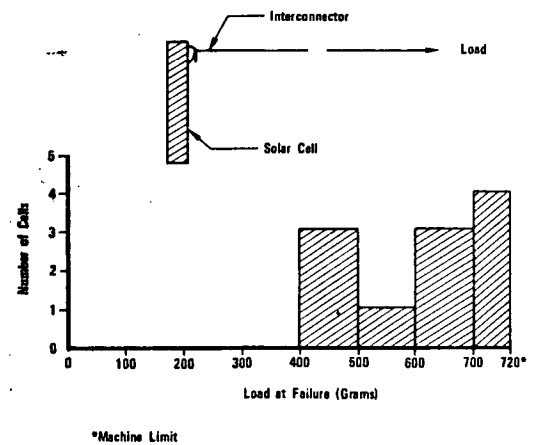


Figure 49. Results of Peel Tests on Thermal-Diffusion Bonded Solar Cell Joints (From Reference 21)

In Reference 16, Eakins reports that Hughes has experienced good results using the thermal compression method to weld silver interconnectors-to-silver contacted cells. Measurements of the dark reverse leakage current to a -10 volt reverse bias have shown that no junction shunt resistance degradation occurred due to the welds.

### SECTION 3

### CONCLUSIONS

The following conclusions result from the study activity which is summarized in Section 2 of this report.

1. It appears possible to design a planar solar array system to meet the 110 watt/kg power-to-weight ratio goal without requiring advances in the state-of-the-art. However, this achievement is contingent upon the effective utilization of existing technology in the areas of ultra-thin solar cells, integral coverglass and welded interconnectors.
2. The continuous longeron coilable lattice ASTROMAST is the lightest weight deployable boom system available for the bending stiffness required for this application. The relatively large canister height required for this mast makes integration into the system more difficult when compared to an equivalent BI-STEM type boom and actuator. A lanyard deployed continuous longeron ASTROMAST would require less stowed height (and lower deployer weight) and should be investigated during the next quarter.
3. The use of boron/aluminum composite as the boom element material in the fabrication of a BI-STEM type boom is weight competitive with the continuous longeron ASTROMAST and requires a considerably lower actuator height. This application for the boron/aluminum monolayer material represents an advancement in the state-of-the-art. A preliminary investigation indicates that it may be feasible if a high strength, heat treatable aluminum alloy such as 7178 were used as the matrix material to achieve the required transverse tensile strength. Development work is required to verify that the BI-STEM section can be formed and heat treated to achieve the temper necessary for the flattening and coiling of the elements. The thermal shock requirement of 1000 cycles between -190 and +140°C may cause problems with the formation of voids within the composite. This aspect can only be explored by additional testing.
4. The "V"-stiffened solar array concept shows the promise of providing increased stiffness to out-of-plane bending when compared to an equivalent planar geometry. This may allow a reduction in the boom stiffness (and weight) required to maintain a specified deployed natural frequency.

## SECTION 4

### RECOMMENDATIONS

Because of the tremendous improvements predicted for the "V" stiffened solar array concept, it is recommended that a simplified model of this concept be constructed to verify the predicted behavior. This model should have a length on the order of 1.5 m (5 ft) and should be capable of being "twang" tested to qualitatively assess the analytical results.

## SECTION 5

### NEW TECHNOLOGY

No items of new technology were reported during this period. The "V" stiffened solar array configuration described in Section 2.4 was identified as a new technology item and a report is being processed.

## SECTION 6

### REFERENCES

1. "Feasibility Study of a 110 Watt per Kilogram Lightweight Solar Array System - Quarterly Report No. 1," GE Document No. 72SD4233, August 15, 1972
2. Coyner, J.V., Jr. and Ross, R.G., Jr., "Parametric Study of the Performance Characteristics and Weight Variations of Large-Area Roll-up Solar Arrays," Technical Report 32-1502, December 15, 1970.
3. Felkel, E.O., Wolff, G., et al., "Flexible Rolled-up Solar Array," Technical Report No. AFAPL-TR-72-61, 30 June 1972.
4. "First Topical Report Update - Evaluation of Space Station Solar Array Technology," LMSC Report No. D159124, July 1972.
5. Crawford, R.F., "Strength and Efficiency of Deployable Booms for Space Applications," AIAA Paper No. 71-396.
6. Private Communication with R.F. Crawford, ASTRO Research, October 25, 1972.
7. "Design and Development of a Thirty Watt per Pound 250 Square Foot Roll-up Subsolar Array - Final Report," GE Document No. 71SD4239, May 20, 1971.
8. Private Communication with E.F. Binz, North American Rockwell, August 22, 1972.
9. Toth, I.J., Brentnall, W.D., and Menke, G.D., Fabricating Aluminum Matrix Composites, Journal of Metals, September 1972.
10. Kreider, K., et al., "Plasma Sprayed Metal Matrix Fiber Reinforced Composites," Technical Report AFML-TR-68-119, July 1968.
11. Kreider, K., et al., "Metal Matrix Composite Technology," Technical Report AFML-TR-71-204, December 1971.
12. MIL-HDBK-5A, "Metallic Materials and Elements for Aerospace Vehicle Structures."
13. Luft, W., "Solar Cell Interconnector Design." IEEE Transactions on Aerospace and Electronic Systems, Vol. AES-7, No. 5, September 1971.
14. Salama, A.M., et al., "Stress Analysis and Design of Silicon Solar Cell Arrays and Related Material Properties," paper presented at the 9th Photovoltaic Specialists Conference, May 1972.
15. Luft, W., et al., "Hardened Solar Array Panel Segments," Technical Report AFAPL-TR-72-33, May 30, 1972.

16. Eakins, T.C., "Results of Solar Cell Welded Interconnection Development," paper presented at 1972 IECEC.
17. Cohen, D.B., and Schwartz, S., "Engineering Study of Elevated Temperature Solar Cell Panel Fabrication Techniques," paper presented at the 8th Photovoltaic Specialists Conference, August 1970.
18. Reinhartz, K.K., and Capart, J.J., "Status of Welded Solar Cell Module Technology at ESRO," paper presented at the 8th Photovoltaic Specialists Conference, August 1970.
19. "Development of a Flexible Solar Cell Panel," a proposal by Messerschmitt-Bolkow-Blohm, Space Division in response to ESRO RFP A0/335, August 24, 1970.
20. Boller, H.W., et al., "Solar Cells and Generator Technology for the Helios Sun Probe," paper presented at the 9th Photovoltaic Specialists Conference, May 1972.
21. Clarke, D.R., "High-Temperature Annealable Solar Array," paper presented at the 7th Photovoltaic Specialists Conference, November 1968.